

AN ABSTRACT OF THE THESIS OF

Travis R. Roth for the degree of Master of Science in Water Resource Engineering presented on 10 December, 2010.

Title: Headwater Stream Characterization: An Energy and Physical Approach to Stream Temperature Using Distributed Temperature Sensing

Abstract approved:

John S. Selker

Headwater streams are an integral part of the ecological health of the greater stream network as they provide valuable biological habitat, provide upwards to 95% of total in channel flow, while providing downstream reaches with important constituents such as sediment and woody debris. Small headwater streams are particularly susceptible to anthropogenic and natural disturbances that affect their runoff production, chemical make-up, and thermal regime. Based on their position in the drainage basin and contribution to stream flow, heat energy transfer within a small mountain stream helps establish the thermal regime of the downstream lower order streams. However, headwater catchment thermal function remains poorly understood. Stream temperature is a manifestation of the environment through which it flows and the mechanisms by which it reaches the stream. Subsurface process controls, such as local soil properties, bedrock topography, and lateral flow discharge play an important role in headwater stream generation.

Study outcomes are a result of vigorous field experimental work at the Watershed 07 (WS07) stream at the H.J. Andrews Experimental Forest (HJA) located in the Western Cascades, Oregon. Bedrock Topography was delineated through the use of a dynamic cone penetrometer, local lateral inflow sources were identified and quantified through the application of a salt tracer, and the energy budget was

characterized through the use of Distributed Temperature Sensing (DTS) technology. High gradient, low volume streams such as WS07 provide unique challenges for DTS deployment which require extensive post-calibration data analysis. An automated cable submersion identification process was developed and was carried out on the collected temperature data with 32.8 % (379 of 1155) of measured temperature points identified as “in-water”. Uncertainty propagation analysis associated with DTS measurement was calculated to be 0.21 °C.

Salt tracer application found that 2 localized lateral inflow discharge to the stream accounted for 15% and 16% of total discharge in the upper section of the stream. Downstream lateral inflows exhibited incremental additions to stream discharge on the order of 5%. Stream discharge increased by 1.13 l/s from the upper section to the start of the lower section, an increase of 45%. Substantial lateral inflows provided reduction of stream temperatures in the lower section.

Using DTS technology we measured stream temperature as a validation method for a physically based energy balance stream temperature model to characterize energy controls on stream temperature. Analysis of model performance was determined through root mean square error with reported values of 0.38 °C and 0.32 °C for the upper and lower section, respectively. Total energy inputs into the upper and lower sections of the stream were 302 W/m² and 210 W/m². Primary energy balance components were found to be solar radiation, atmospheric longwave radiation, and bed conduction. Solar radiation accounted for 63% of total energy flux into the stream in the upper section and 28% in the lower section. This is primarily a result of the distinct vegetation differences between the two reaches. Atmospheric longwave radiation contributed 27% and 26% of total energy flux in the upper and lower sections, respectively. While bed conduction made up 11% and 24% of the total flux in the upper and lower sections.

© Copyright by Travis R. Roth
10 December, 2010
All Rights Reserved

Headwater Stream Characterization: An Energy and Physical Approach to Stream
Temperature Using Distributed Temperature Sensing

by

Travis R. Roth

A THESIS

Submitted to

Oregon State University

In partial fulfillment of
the requirements for the
degree of
Master of Science

Presented 10 December, 2010

Commencement June 2011

Master of Science thesis of Travis R. Roth presented on 10 December, 2010.

APPROVED:

Major Professor, representing Water Resource Engineering

Director of the Water Resources Graduate Program

Dean of the Graduate School

I understand that my thesis will become part of the permanent collection of Oregon State University libraries. My signature below authorizes release of my thesis to any reader upon request.

Travis R. Roth, Author

ACKNOWLEDGEMENTS

Just as stream temperature is a reflection of the landscape through which it flows, I am a product of my personal landscape. This landscape isn't just the physical surroundings in which I find myself but rather it includes the people that I care about and those who have cared for me. There are many who have helped in myriad ways in my development as a scientist. There are those who have shaped me as the person I am today. And there are those who have shared with me their life, laughter and love. Some have been exclusive to one of the above groups, while many are included in them all. As I finish this step in my life and prepare to take the next I would like to acknowledge you all. Thank you.

23 December, 2010
Thistle Dew Cabin, Wyoming

Travis R. Roth

TABLE OF CONTENTS

1. Introduction.....	1
2. Headwater systems.....	2
2.1. Definition.....	2
2.2. Project goals and hypothesis	4
2.3. Overview of research plan	5
3. Stream Temperature.....	6
3.1. Literature review of current understanding	6
3.2. Energy controls	7
3.3. Topographic and geomorphic controls.....	11
4. Study Site.....	13
4.1. H.J. Andrews Experimental Forest	13
4.2. Watershed 07.....	14
5. Methodology.....	16
5.1. DTS.....	16
5.2. Data processing.....	18
5.3. In or out of water identification	20
5.4. Measurement uncertainty	31
5.5. Model structure.....	36
5.6. Model calibration parameters and sensitivity analysis	36
5.7. Tracer study	37
5.8. Bedrock topography and soil property methods.....	41
5.8.1. Knocking pole.....	41
5.8.2. Soil cores, soil particle distribution, and hydraulic conductivity methods.....	43
5.9. Meterological stations and other measurements	45
6. Results.....	46
6.1. Tracer results.....	46
6.2. DTS results.....	51
6.3. Soil characterization.....	63
7. Discussion.....	70
8. Conclusion.....	73

9. References.....	77
10. Appendix.....	83

LIST OF FIGURES

<u>Figure</u>	<u>Page</u>
Figure 1: H.J. Andrews Experimental Forest geographical location	14
Figure 2: WS07 Boundary, stream, gauge house, and Hi-15 Met Station locations	15
Figure 3: Schematic of the OFS Mini LT Flat Drop Fiber Optic Cable construction (AFL Telecommunications)	17
Figure 4: Time series of WS07 temperature profile. Red circles indicate examples of the out of water sections	22
Figure 5: “Shoulder” example of headwater stream with DTS cable partially submerged. Each color represents a single temperature measurement in time	25
Figure 6: Dataset after out-of-water cable sections are eliminated. Dark blue areas are areas that were deemed to have been out of water	27
Figure 7: Bulk Salt Concentration for each location along the stream length	46
Figure 8: Change as percent of total discharge at each location (l/s) along the stream	48
Figure 9: Calculated discharge for each location (l/s) along the stream	49
Figure 10: Longitudinal profile of WS07 stream of specific conductance vs. time vs. stream temperature	51
Figure 11: DTS measured stream temperature. Dark blue represents the subsurface portion of the stream. Vertical striations are result of linearly interpolated measurements of in water sections. The pronounced horizontal striation during day three is from a power supply outage	52
Figure 12: Temperature profiles of the points along the stream where A) the stream goes subsurface and B) downstream resurface point	53
Figure 13: Simulated model temperature in space and time (x and y axis). Dark blue section represents the subsurface portion of the stream	54
Figure 14: Upper section at downstream boundary modeled versus observed temperature (°C) profile for the study duration	55

LIST OF FIGURES (continued)

<u>Figure</u>	<u>Page</u>
Figure 15: Lower section at downstream boundary modeled versus observed temperature (°C) profile for the study duration	56
Figure 16: Discharge calculated from salt dilution and DTS measurements	59
Figure 17: Calculations of $1/f$ and $1/g$ in equations 49 and 51	62
Figure 18: WS07 knocking pole depth to bedrock surface layer at each location	63
Figure 19: WS07 Slope angle versus depth to bedrock at each knocking pole location	64
Figure 20: Soil Resistance for 5 knocking pole site locations. An expressed exponential increase of resistance with depth is present	68
Figure 21: Conceptual drawing of WS07 subsurface water interaction. Hyporheic exchange as well and groundwater inclusion is shown to play a large role in the WS07 temperature regime. Also of note is the differences in vegetation in the Upper and Lower sections of the watershed	71

LIST OF TABLES

<u>Table</u>	<u>Page</u>
Table 1: OFS Mini Flat Drop Specifications	18
Table 2: SensorTran M04 5100 Product Specifications	18
Table 3: One hour temperature measurement standard deviations of randomly selected sections of cable under differing canopy cover densities, as represented by their θ_{VTS} , and depth of water column	30
Table 4: Post-Model Calibration Model Parameter Values for D_F , θ_{VTS}	37
Table 5: Average Energy Balance Components for both Sections of River, computed for 1:00-3:00 pm during July 13 th -15 th 2010	56
Table 6: Average Soil Particle Size Distribution (%) from the 11 sample sites	65
Table 7: K_{SAT} values (m/s) from soil cores at various depths using the constant head method	65
Table A1: Knocking pole ID, name, GPS position, and soil depths	84
Table A2: Hydraulic conductivity measurement ID, name, GPS position, and K_{SAT}	85

1. Introduction

Headwater catchments are the origins of stream networks and, as such, characterizing their ecological, biological, and physical function is necessary to understand downstream processes. Small mountain headwater streams provide valuable biological habitat for a variety of communities (Hack and Goodlett, 1960). Due to their small size they are particularly responsive to natural and anthropogenic change, including forest management practices, debris flow disturbances, and climate regime (MacDonald and Coe, 2007). These disturbances can affect their runoff production (Jones, 2000), stream thermal regime (Johnson, 2004), chemical weathering rates (Likens et al., 1977), and fish habitat (Dietrich and Anderson, 2000). Headwater streams also provide other important constituents to downstream reaches, including sediment, woody debris, organic matter and nutrients. Because of their inherent linkage with downstream water resources, headwater systems are an important, yet relatively poorly understood, ecosystem.

In Oregon 1,397 streams are listed as impaired under the Clean Water Act 303(d) for a variety of reasons, including but not limited to adverse affects from mineral extraction, logging, dams, and urban development (US EPA, 2006). Increasingly, stream temperature is seen as the foremost cause of stream degradation and subsequent 303(d) listing. This poses a serious risk to many Oregon fish species, including salmon, which rely on cool water to survive in headwaters as they prepare to spawn. Stream temperature manifests a combination of multiple energy and mass transfer processes. Stream temperatures tend to increase in the downstream direction as surface water is exposed to external energy sources. These processes in headwater catchments are temporally dynamic, often with various energy fluxes dominating the energy budget at different times. Determination of the controls on stream temperature in headwater systems is essential for downstream management of our water resources and to prepare resource management for an uncertain future. The Pacific Northwest region has a long history of forest timber harvest. Forestry was a primary economic driver of the region for much of the 19th and 20th centuries

providing much of the timber for the rest of the United States. As a result the industry expanded onto larger parcels of both private and public lands. By late 20th century , with more and more land in the region coming under production each year, the timber industry, local communities, and public research organizations came together to understand forest management practices and how they affect downstream water quantity and quality. Understanding that the forest was a finite resource, these groups sought how to manage the forests in an environmentally and economically viable way.

Despite the extensive research on the subject of the thermal impacts of forest practices on water resources, it is still vigorously debated in the region. One significant result that has come out of this debate was that in order to help mitigate adverse affects of forest harvesting on stream temperature the establishment of a riparian buffer exempt from harvest along the stream length must be included. The riparian buffer represents a small area, typically 1-5m on either side of the stream, for the entire length of the stream channel. While this buffer is required for larger fish bearing streams, often smaller, i.e. headwater streams, are afforded less protection under current legislation (Young, 2000).

In addition to the importance of energy transfer of surface water stream temperatures, the physical, chemical, and biological features of headwater stream function are critical to overall down-stream ecological health. With this in mind, we explored the temperature regime of a small headwater catchment at the H.J. Andrews Experimental Forest in the western Cascades, Oregon. We set out to establish a physical understanding of stream temperature controls and the processes that explain the energy budget of these unique ecosystems through distributed temperature sensing (DTS) fiber optics, hydrometric analysis, and modeling.

2. *Headwater systems*

2.1 *Definition*

Headwater systems constitute the uppermost portions of a stream network and are typically considered to be made up of the first- and second-order streams (Gomi et al., 2002; Meyer and Wallace, 2001) as hillslope source water emerges to form stream channels. These headwater streams typically have small drainage areas <2km (Adams and Spotila, 2005). Headwater streams comprise the vast majority of larger basin drainage networks and approximately 95% of all in-stream channel flow is generated by hillslopes and headwater streams are the primary source of streamflow (Moore et al., 2005). Routing of hillslope water to the stream channel occurs from a variety of mechanisms, including infiltration excess overland flow, subsurface storm flow, and groundwater. Infiltration excess overland flow, however, is rare in forested catchments with high infiltration capacities such as the forests of the Cascades. The Oregon Headwaters Research Cooperative has defined headwater streams as those that have an average annual stream flow of less than 2 ft³/s in Western Oregon, and have a bankfull width range from less than 1m to 3m (OHRC). These systems represent the majority of the total stream length within most catchments, draining 70-80% of the total catchment area (Horton, 1945; Schumm, 1956; Shreve, 1969; Sidle et al., 2000). Their upstream delineation is defined as areas where sufficient surface runoff is concentrated to cause scour and distinct banks (Dietrich and Dunn, 1993). Whereas the downstream end of headwater catchments or lower boundary is more ambiguous, but has been defined in the literature as the colluvial-alluvial transition point, usually between a channel slope of 20 to 30% (Montgomery and Foufoula-Georgiou, 1993; Woods et al., 1995; May and Gresswell; 2004).

The formation of headwater channels is not relegated to perennial streams, as snowmelt or persistent rainfall may induce sufficient surface runoff to form ephemeral channels. At the initiation point channels easily migrate in response to storm events or severe disturbance (Montgomery and Dietrich, 1989) although variation in initiation location is not enough to disrupt stream order. Stream channel initiation location is influenced by the lithology of the underlying substrate, soil

characteristics, climate regime, and land use (Montgomery and Dietrich, 1988; Prosser, 1996; Wemple et al. 1996).

2.2 *Project Goals and Hypothesis*

Major river systems all have their origins in headwater catchments. This inherent link to the upslope origins and how these headwater characteristics are translated downstream is important to understand so as to equip water resource managers with the tools required to adapt to future climate scenarios as they develop. The connectivity of headwater systems to down gradient, lower order stream is poorly understood. How does the thermal regime in headwaters connect to the downstream catchment and what are the primary controls on this transfer of surface water energy? As our mountain water resources move towards an uncertain future, via changes in snow accumulation, precipitation type, and melt timing, understanding headwater catchment function is ever more important. It is with this in mind that we set out to examine the thermal regime of a headwater catchment. We ask: how is stream temperature associated with upstream physical and heat energy transfer processes within a small headwater catchment? What are the thermal controls on surface water systems and what role does the subsurface play in headwater stream generation and stream discharge.

The following is a study focusing on stream temperature dynamics at the catchment scale in a headwater system. The goal of this study was to investigate the process controls on stream temperature through the coupling of high resolution temperature monitoring technology and a physically based energy model. Catchment water storage and release play a significant role in stream temperature. To investigate the role of subsurface processes in headwater function we sought to characterize the bedrock topography and soil properties. The dynamic coupling of surface and subsurface water is clear in headwater catchments and as such we sought to examine this interaction through an application of a conservative salt tracer. Finally, we looked into the physical controls on energy transfer through a high resolution stream

temperature monitoring and modeling effort. The compelling reason behind the research was the considerable deficiency in process based understanding of headwater catchment function on stream temperature.

2.3. Overview of research plan

Each component of the study was designed to explore one aspect of the temperature function of headwater catchments and taken together gives us insight into the catchment function as a whole. High spatial and temporal resolution distributed temperature sensing (DTS) technology was employed to characterize stream temperatures and detect groundwater lateral inflows. A conservative tracer application sought to identify groundwater interactions and to independently verify DTS identified sources. Hydrometric measurements included soil property characterization and bedrock topography field surveys of the subsurface environment. And finally DTS measurements were also used as a verification tool for a physically based energy balance model with the goal to understand the influence of climatic forcings and examine their impact on stream temperature.

The influence on stream temperature of subsurface water with surface channel flow is significant and apparent in headwater catchments. Examining this interaction through process based experiments and modeling allows for tractable understanding of headwater systems. While we know on a coarse scale how energy fluxes induce temperature change in streams, there has been little applied research into headwater stream temperature response to potential climate and environmental change (Dent et al., 2008). The importance of headwater systems on the downstream stream thermal regime is less understood and understanding the headwater stream temperature response to climate forcings is vital to better determine impacts on downstream water resource management. New technologies for hydrological measurement have emerged recently that have fundamentally changed the way we can 'see' catchment function (Selker et al., 2006a, Berman et al., 2009). These new technologies can be utilized to formulate hypotheses regarding how surface and subsurface interaction

function at the headwater catchment scale. High resolution highlights areas of our understanding that have been masked before through coarse scale measurement sampling protocols.

The research paper below follows a logical format that first presents a detailed review of the two main components of the research plan stream; stream temperature dynamics and catchment scale stream generation, a presentation of the methodology used follows, and finally results and discussion of the research are presented.

3. *Stream Temperature*

3.1 *Literature review of current understanding*

The Pacific Northwest region has a long history of stream temperature research due to the regional importance placed on salmon bearing streams which require cool temperatures and the intimate history of forest logging practices. Stream temperature is a temporally and spatially diverse function of a catchment and is the manifestation of local environment heat energy fluxes. Stream temperature directly influences the health of a stream and the ecosystem it dissects. With regards to biological activity within a stream the temperature affects metabolic rates, physiology of aquatic species, the solubility of oxygen and other gases necessary for biological activity, and helps determine rates of nutrient cycling and productivity (Allan, 1995). It also exerts a strong influence on many physical characteristics of water such as vapor pressure, viscosity, density, and surface tension (Stevens et al., 1975). Stream temperature is directly proportional to the heat energy within the system and water volume. Water with more energy contained within it has a higher temperature.

$$\text{Water temperature} \propto \text{heat energy/water volume} \quad \text{Eq. 1}$$

It is therefore apparent that a stream temperature is dependent on both the heat load and the stream discharge and any factor that alters either will ultimately influence the stream temperature regime (Poole and Berman, 2001). Water temperature is highly sensitive to anthropogenic and natural activities, and is critical to aquatic ecological processes, which make it an important parameter of water

quality. The spatial variability of stream temperatures along the longitudinal profile of stream length is considerable, with the generally accepted view that summer-time stream temperatures rise with distance from channel formation. The rate of increase however is dependent many local processes. These processes are comprised of external drivers acting on the water itself, i.e. energy, the internal structure of the integrated stream system (channel structure, vegetation) and the alluvial aquifer (Poole and Berman, 2001). Sullivan and Adams (1991) go further in saying that climatic forcings as well as stream morphology, groundwater influences, and riparian canopy cover are the primary determinants of stream temperature.

3.2 Energy controls

Heat energy balance of a stream is comprised of the net heat transfer between the water and the atmosphere and the net heat transfer between the water and the substrate (Boyd and Kasper, 2003). Heat transfer between the water and atmosphere is through four main processes: heat input from solar radiation, net longwave radiation, evaporative heat loss (latent heat), and convection (sensible heat). Heat transfer between the water and the streambed is governed by conduction. This can be expressed through a simple energy balance equation:

$$\phi_{Stream} = \phi_{Radiation} + \phi_{Longwave} + \phi_{Latent} + \phi_{Sensible} + \phi_{Conduction} \quad \text{Eq. 2}$$

where ϕ_{Stream} equals total heat energy flux [W/m^2], $\phi_{Radiation}$ is the direct incoming solar radiation, $\phi_{Longwave}$ is the net longwave radiation, ϕ_{Latent} is the latent heat flux, $\phi_{Sensible}$ is the sensible heat flux, and $\phi_{Conduction}$ is the bed conduction (Boyd and Kasper, 2003).

The components of the energy balance are either directly measured through instrumentation in the field or through computed reference measurements based on empirical methods from climate variables. Energy balance components, especially atmospheric forcings, vary both temporally and spatially making measurement

resolution and placement within the catchment important. Limitations however, exist such as instrumentation cost and site accessibility forcing most studies to use a single meteorological station for climate input measurements which are then scaled accordingly.

Energy budget research below forested canopies has been conducted for decades due to the timber harvest industry and the need for understanding the impact of harvesting practices on downstream water resources. From this extensive breadth of empirical studies it has been widely reported, based on these field data and model simulations, that direct solar radiation is the main energy balance component affecting stream temperature (Brown, 1970; Sinokrot and Stefan, 1993; Johnson, 2004). Solar radiation passing through the atmosphere and striking the earth's surface represents an average of 19% of total solar radiation while an additional 28% can be described as scattered or diffuse solar radiation (Trewartha, 1968). It is generally accepted that a correlation between air temperature and stream temperature exists, reflecting the common factors which heat both systems, and the exchange of energy between these landscape elements (Mohseni and Stefan, 1999; Ozaki et al., 2003).

In mid-latitude catchments, during the hottest time of the year, direct solar radiation contributes up to 80% of the total flux in the energy budget (Montieth and Unsworth, 1990). Given the magnitude of solar radiation within the energy budget many researchers have shown the importance of riparian vegetation cover to limit stream exposure to direct solar radiation and thus reduce or limit stream temperature augmentation (Poole and Berman, 2001; Johnson 2004; Roth et al., 2010). Johnson (2004) conducted a shade experiment where a plastic was placed over a 200m exposed stretch of stream to provide simulated shading. Results showed a decrease in maximum stream temperatures at the downstream end of the shading experiment as a direct result of the reduction of solar energy flux into the stream. While Roth et al. (2010) used a modeling approach to determine that in-channel vegetation (e.g., reeds) can provide riparian shading which is effective in reducing stream temperature.

Topographical location and stream morphology can also influence on the amount of solar radiation that reaches the stream surface. In narrow, incised channels the stream bank may act as shade and effectively reduce incident radiation (Webb and Zhang, 1997). Whereas large wide streams tend to have a canopy gap overhead which increases the amount of solar radiation at the stream surface, this is especially evident in north-south oriented streams (Beschta, 1997). In areas with solar elevation angles greater than 30 degrees, only a small portion of incident solar radiation is reflected by the stream surface, leaving 90-95% available to heat the stream (Oke, 1987, Evans et al., 1998).

The remaining components of the energy balance (net longwave radiation, streambed conduction, sensible, and latent heat transfer) are considered secondary controls because their relative magnitude is typically less than solar radiation within the energy budget. The effects of these parameters on individual energy balance components are varied and are sight specific.

Longwave radiation is defined as the radiant flux resulting from the emission of the atmospheric gases and the land and water surfaces of the Earth (Brutsaert, 2007). Terrestrial materials have a considerably lower temperature than the sun, and as such the radiation they emit has longer wavelengths, almost all within the range of 4-100 μm whereas solar shortwave radiation is contained within the wavelength range from 0.1 to 4 μm . Longwave radiation is difficult to measure directly so it is usually calculated from other empirically derived equations that include more readily measured inputs. Its effect on stream temperatures is dependent on vegetation densities and cover within the riparian zone. Reifsnnyder and Lull (1965) show that longwave radiation reaching the forest floor increases with increases in canopy density due to the warmer forest canopy relative to the overlaying atmosphere. Bed conduction importance is highly influenced by substrate type (Johnson, 2004). Conduction is a function of temperature differences between the underlain substrate and the water and the rates of temperature exchange are dependent upon the thermal conductivities of the bed material. Bed conduction in stream channels that

include extensive exposed bedrock is more influential on the thermal regime of a stream than alluvial channels, by suppressing diurnal temperature fluctuations through absorbing heat energy during the day and releasing the stored energy during the cooler night (Brown, 1969; Beschta and Weathered, 1984). However, for shallow broad streams, exposed bedrock may have the opposite effect and induce higher extreme temperatures and enhancing diurnal fluctuations through direct absorption of solar energy by the bedrock surface and delivering this energy into the stream, and the rerelease of stored energy at night is minimal, while the stream's loss of energy via long-wave radiation may considerably cool the stream (Johnson and Jones, 2000; Johnson, 2004).

The turbulent heat fluxes relating to latent and sensible heat are associated with the heat loss/gain with phase changes of water (latent heat) and with energy transfers that affect the surrounding air temperature (sensible). Latent heat, the exchange of energy via evaporation and condensation, is controlled by a combination of processes involving the humidity gradient, atmospheric stability, and wind-speed in the air parcel above the stream. Evaporative heat loss occurs where the vapor pressure at the water surface exceeds that of the vapor pressure in the overlaying air. Conversely, condensation heat gain occurs where the vapor pressure of the air exceeds the vapor pressure at the water surface (Moore et al., 2005). Vapor pressure of the air is a function of the processes affecting the stream's surrounding air mass; for instance because the peak air temperature under forest canopies are generally cooler than forest-free areas, the relative humidity is typically 5-25% higher, reducing the rate of evaporative heat loss (Chen et al., 1995; Brosofske et al., 1997; Davies-Colley et al., 2000; Spittlehouse et al., 2004).

Sensible heat transfer depends on the temperature difference between the water surface and the overlaying air and the wind speed. Where the strongest temperature gradients exist, the heat transfer is the greatest. When the stream is warmer than the overlaying air mass, heat transfer away from the stream is supported by the unstable air, increasing the temperature gradient which then increases

turbulence. When stable air conditions exist, i.e. when the stream is cooler than the air mass, heat transfer is low due to the dampening of turbulence (Oke, 1987). Because both turbulent heat fluxes are dependent on a wind function, there is a likelihood of high uncertainties associated with the computed values. This is particularly the case for wind measurements under canopies when mean wind speed are measured from anemometers in open areas (Story et al, 2003). The limiting factor of turbulent heat transfer over small streams is the lack of ventilation (Brown, 1969; Webb and Zhang, 1997; and Story et al., 2003). Typical values of sensible and latent heat exchanges are estimated as an order of magnitude lower than net radiation on sunny days (Brown, 1969; Moore et al., 2005).

3.3. Topographic/geomorphic controls

Catchment structure and geomorphology play a large role in determining stream flow and temperature. Stream discharge is ultimately derived from precipitation, but the storage and release mechanisms depend upon catchment topographical and physical characteristics prior to the point where the water has reached the stream channel. Soil characteristics, catchment topography, vegetation type and density, and bedrock properties all have significant effect on water pathways, pre-channel losses of water, and routing through the subsurface and delivery to the stream channel. In their seminal work on source area concepts, Hewlett and Hibbert (1967) stated the importance of surface topography on stream water delivery in the form of the variable source area concept. Landscape topography in steep mountain catchments have a large elevation potential energy component which can dominate hydraulic potential and is the principle variable of water distribution (Beven and Kirkby, 1979; Anderson and Kneale, 1982). Topographic characteristics of a catchment can help explain the residence time distribution of water. McGuire et al. (2005), showed the importance of flow path length and flow path gradient on catchment water mean residence time, two simple topographical characteristics taken from digital elevation models (DEM). Their study suggested that residence times are inversely proportional to flow path

gradient and directly proportional to flow path length. These topographical attributes represent the distance and gradient along each flow line within a catchment where water enters the stream. Groundwater discharge also plays a major role in stream temperature as this alters the volume of surface water and is usually discharged with lower heat energy than surface water.

In small headwater catchments the near-stream riparian zone may be relatively small due to topographical constraints that steep gradient slopes incur and limited surface stream channel. Riparian zones, however constrained by topography, often have elevated water tables which results in higher soil moisture. The increased soil moisture allows riparian forest cover and vegetation to differ from elsewhere in the catchment where hydrological conditions inhibit certain plant growth. The higher soil moisture, dense forest cover, and the stream water itself provides for a localized elevated water vapor content and acts as a heat sink during the day (Moore et al., 2005). Additionally, riparian zone vegetation cover transpires during the day, further contributing local water vapor (Danehy and Kirpes, 2000).

Local characteristics of the stream location within the landscape have significant effect on energy budget components. For example forest cover density, type, and maturity can influence the thermal regime of the riparian area, including the stream itself. Forest cover tends to reduce wind speeds to 10-20% of the wind speeds in large openings (Raynor, 1971; Chen et al., 1995; Davies-Colley et al., 2000). This reduction of wind speed within the riparian zone reduces the turbulent flux which has an effect on evaporation rates. Underneath these canopies the diurnal air temperature range is also reduced compared to open areas with maximums being up to 6°C lower than open areas and about 1°C warmer at night due to longwave radiation emission from the canopy (Chen et al., 1995; Spittlehouse et al., 2004.) Local landscape influenced parameters within a headwater system can play a major role in stream temperature and are important components within the energy balance.

Stream temperature is a result of complex interactions of the landscape through which the stream flows and both the internal and external energy balance controls

within the catchment. While solar radiation is the principle energy balance component in almost every study to date, the understanding of stream morphology, riparian vegetation, and local microclimate meteorological energy exchange is fundamental to our advancement of knowledge of headwater catchment stream function. The remainder of this paper looks at the present study first by providing the reader with a context of location through a site description, our research methodology, followed by a presentation of the results and accompanied discussion of the findings.

4 Study Site

4.1. H.J. Andrews Experimental Forest

The H.J. Andrews Experimental Forest (HJA) is one of 24 major ecosystem research sites funded through the National Science Foundation as part of the Long-Term Ecological Research program. The Andrews is a 64 km² basin located in the Western Cascades Mountains of Oregon, USA (44.2 °N, 122.25 °W) and drains Lookout Creek, a tributary of the Blue River and McKenzie Rivers (Figure 1). The site began as a basic watershed research station that focused on forest management treatments in 1948. The location of the Andrews was chosen for its broad representation of the greater Cascades with its rugged mountains, steep hillslopes, and diverse ecosystems. Elevation ranges from 410m at the headquarters to 1754m at its highest point. The complex terrain and large ecological diversity has provided HJA researchers with a rich setting to conduct important ecological research. In particular, the HJA has become a center for old-growth forest research globally, resulting from its work on the habitat of the North Spotted Owl in the 1970's which led to a paradigm shift regarding old-growth forest habit and protection measures within the Pacific Northwest and beyond (Forsman et al., 1977). The forest management plan is active with recent forest harvests while protecting areas of stands ranging of >500 yrs old growth dominated by Douglas fir (*Pseudotsuga menziesii*), western hemlock (*Tsuga heterophylla*), and

western red cedar (*Thuja plicata*) and upper elevation forests also include noble fir (*Abies procera*), Pacific silver fir (*Abies amabilis*).

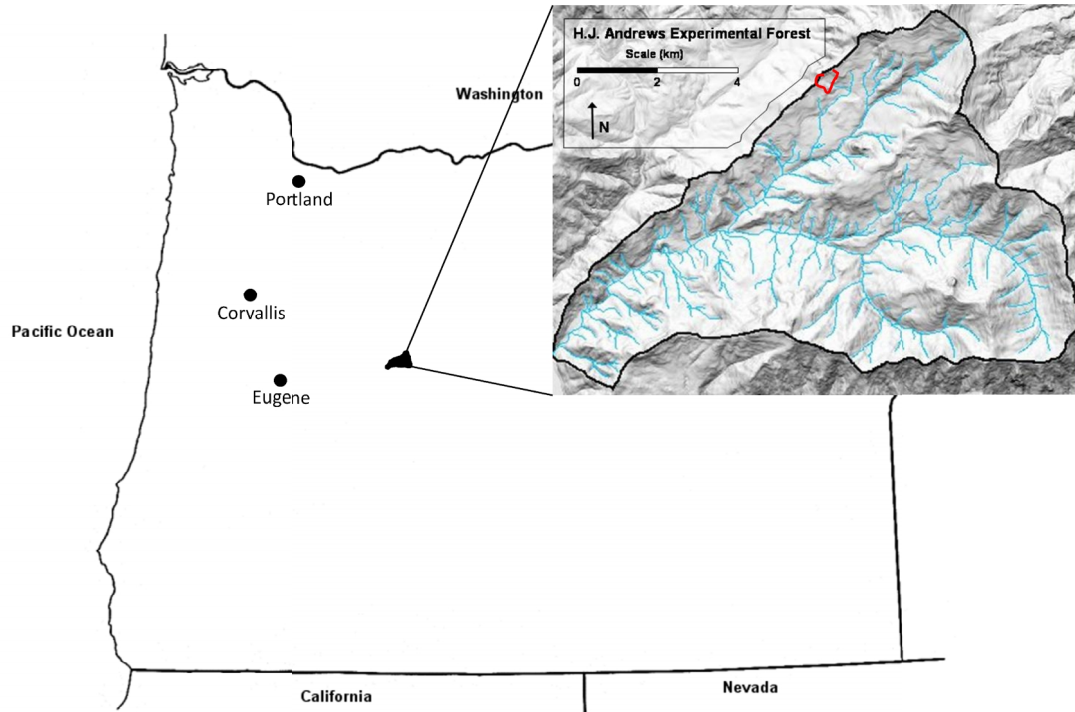


Figure 1: H.J. Andrews Experimental Forest geographical location.

4.2. Watershed 07

At 930m at its outlet, Watershed 07 (WS07) is located within the snow-rain transition zone where numerous cycles of snow accumulation and melt occur with a high frequency of rain-on-snow events, Figure 2. WS07 has a temperate maritime climate with wet mild winters and cool dry summers. The mean annual precipitation is 2122 mm (1999-2008 average) about 80% of which falls between October and April during long duration, low to moderate intensity frontal storms.

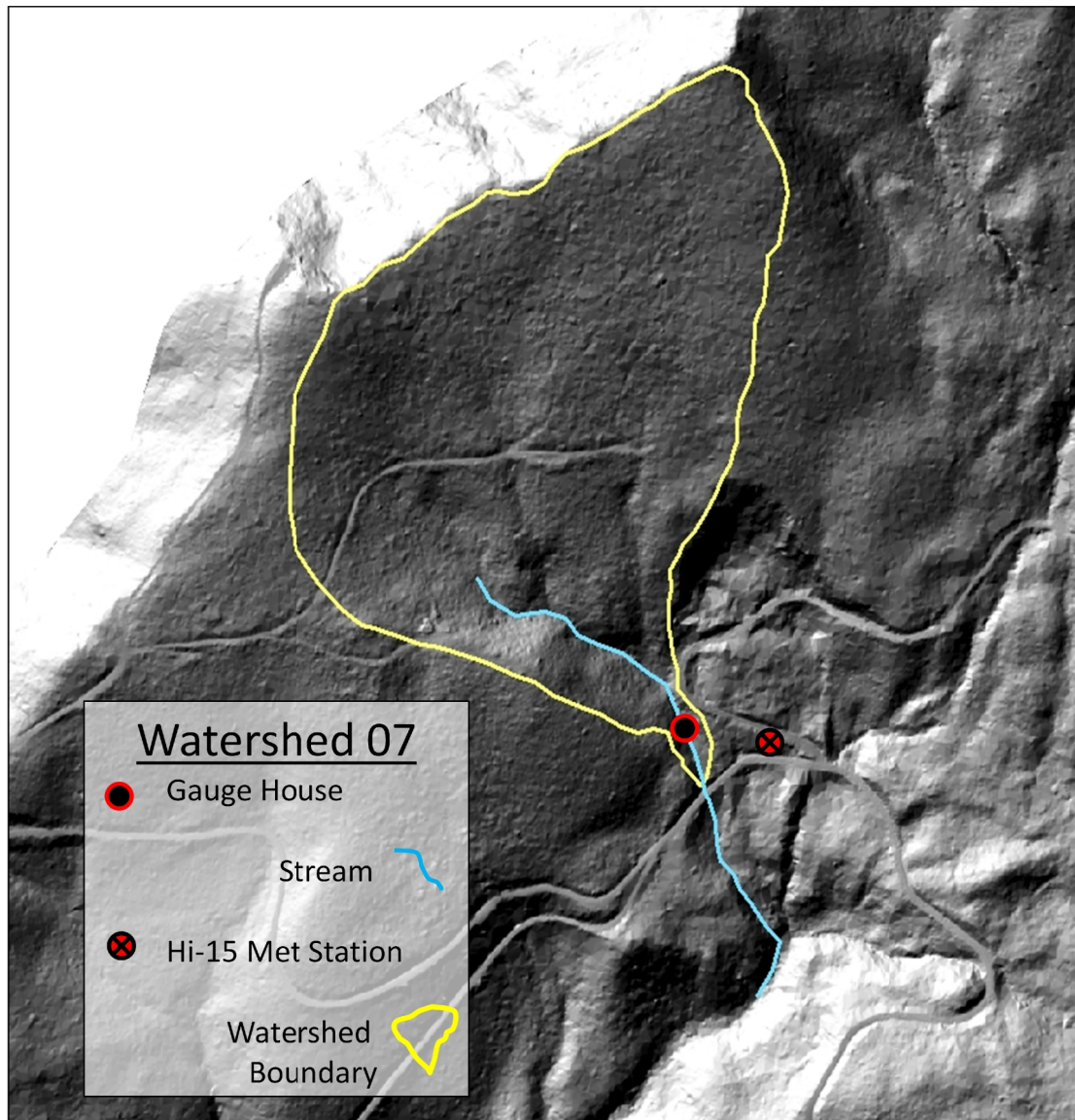


Figure 2: WS07 Boundary, stream, gauge house, and Hi-15 Met Station locations.

The soils of WS07 have been described as predominately comprised as Carpenter and Blue River soils (Dyrness and Hawk, 1972) which are derived from poorly developed Inceptisols with local areas of Alfisols and Spodosols. These soils have thick organic layers that have developed over highly weathered basaltic breccia parent materials (Dyrness, 1969; Legard and Meyer, 1973; Ranken, 1974). The soils have high infiltration rates (typically >500 cm/hr), high drainable porosity (between 15% and 30%), and sharply declining water retention curves (Dyrness, 1969; Ranken, 1974; Harr, 1977).

The bedrock is within the transition between welded and nonwelded ash flows to basalt and andesite lava flows of Pliocene age (Sherrod and Smith, 2000). Additionally, glacial, alluvial, and mass movement processes have created deeply dissected, locally steep drainage systems and variable regolith depth (Swanson and James, 1975). WS07 is characterized by more gentle (11 to 22°) and longer hillslopes (>250 m).

5 *Methodology*

5.1. *DTS*

Physical description

Temperature measurement within WS07 was carried out by use of DTS technology. DTS employs fiber optic cables to measure temperature at high resolution both temporally and spatially along the length of the cable. When light pulses of a specific wavelength are sent down the fiber optic cable a measurable part of light is reflected back along the cable, a process called Raman-backscatter. By timing the return time of light the distance can be calculated. The vast majority of the light pulse is reflected back to the source at the original wavelengths, however some is absorbed by the fiber optic cable and re-emitted at shorter and longer wavelengths than the incident light pulse. Those wavelengths longer than the original are termed Stokes backscatter and those shorter are termed Anti-Stokes backscatter. Anti-Stokes amplitude is exponentially dependent on temperature. By measuring the Stokes/Anti-Stokes ratio temperature measurements can be calculated along the cable length. The temperature point is then averaged at a specified spatial and temporal scale along the entire cable, typically 1m and between 30s to 1hr (Selker et al., 2006a).

DTS technology has its roots in the oil and gas industry in the 1980's when it was primarily used in application for measurement of important factors such as temperature, pressure, strain, flow, and seismic signals (Kragas et al., 2001). Recently however, it has successfully been applied to the ecological setting (Selker et al., 2006b). DTS has also been used to characterize spatial and temporal variation of cold

air drainage within steep slope mountainous catchments (Selker et al., 2008); soil moisture detection within an agricultural setting (Sayde et al., 2010); surface/subsurface interaction locations for identification of hyporheic exchange induced thermal refugia (Collier, 2008); stream restoration effectiveness (Huff, 2010); determination of best management practices in land-use decisions (Roth et al., 2010); and snow cover dynamics (Tyler et al., 2009).

We employed a SensorTran 5100 M4 DTS system for our temperature monitoring applications. DTS installation included deployment of a 1.3 km fiber optic cable within the stream channel at WS07 at the H.J. Andrews. The high gradient catchment with variable seasonal flows which induce mass transport of both sediment and small woody debris were well suited to the use of the OFS Mini LT Flat Drop cable, a highly durable, compact, and lightweight fiber optic cable (AFL Telecommunications, Duncan, SC, USA).

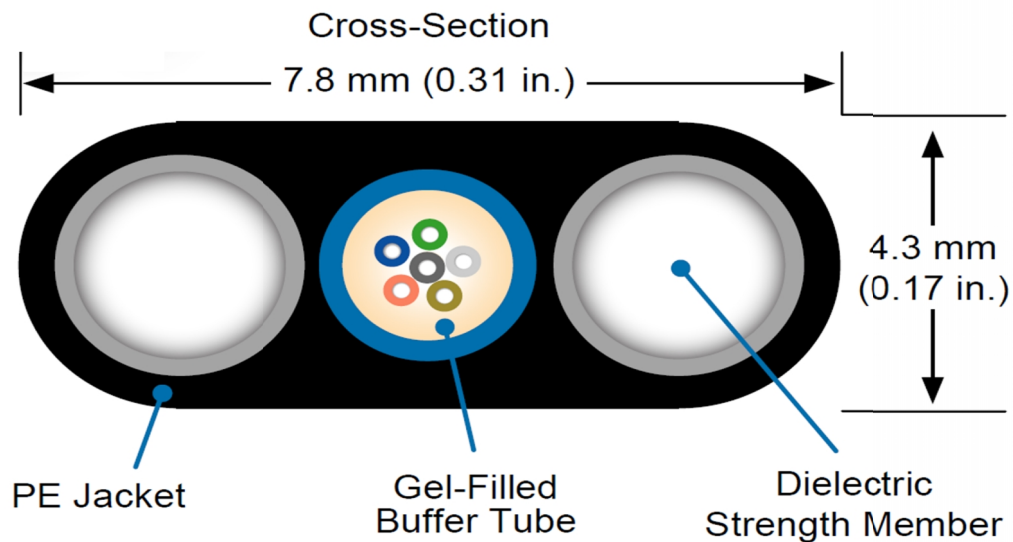


Figure 3: Schematic of the OFS Mini LT Flat Drop Fiber Optic Cable construction (AFL Telecommunications).

The cable construction consists of two, multimode 50/125mm optical fibers placed within a central 2.0 mm gel-filled buffer tube (Figure 3). To provide for tensile

strength and crush resistance two fiberglass rods are placed on either side of the fiber core, all of which are encased in a durable and distance-marked injection-molded black outer polyethylene jacket, weighing a total of 32 kg/km. Table 1 summarizes the cable specifications.

Table 1: OFS Mini Flat Drop Specifications

Cable Dimensions	4.3 mm x 7.8 mm
Cable Weight	32 kg/km
Minimum Bend Radius, With Load	15 cm
Minimum Bend Radius, With No Load	7.5 cm
Maximum Rated Cable Load	1335 N
Maximum Long Term Load	667 N
Temperature:	Installation: -30 °C to 60 °C Operation: 40 °C to 70 °C

The SensorTran 5100 was set-up to at a spatial resolution of 1 m along the cable at 15min time measurement intervals. See Table 2 for key specifications of the SensorTran 5100 DTS system.

Table 2: SensorTran M04 5100 Product Specifications

Spatial Resolution	1m across entire Measurement Range
Sampling Resolution	0.5 m across the entire Measurement Range
Temperature Resolution	Below 0.2°C
Accuracy	Down to +/- 1.0°C without external reference baths
Measurement Speed	>3 s. Dependent upon Temperature Resolution
Measurement Range	Up to 4km per channel
Measurement Temperature Range	-190°C to +700°C

5.2. *Data processing*

Interpretation of reported DTS temperature measurements require an understanding of the principles of the system to minimize temperature measurement uncertainties. Though DTS machines have an internal calibration, additional procedures are required to ensure the accuracy of measurements. Stream studies require field measurement of the actual temperature of reference sections of cable

using known temperature profiles. The protocol designed to establish calibration parameters is presented below.

Cable calibration

DTS cables are incremented with meter marks (MM) which allow for identification of the spatial location of a measurement along the cable length. To ensure correct attribution of measurements to actual locations, GPS coordinates were recorded every 10m along the length of the cable, and the associated MM were noted. DTS temperature measurements also have to be spatially registered with the MM. This was done by associating DTS recorded locations of points where the cable was manually cooled using ice packs during peak air temperatures.

After geo-spatially collocating DTS measurement outputs with stream position the collection of temperature measurements took place. The SensorTran unit has an internal calibration that uses reference coils to correct for temperature offset in temperature measurements. However, this internal correction does not allow for correction gain or attenuation ratio. Examples of factors that affect gain, offset, and attenuation are the quality of connections and fusion welds (splices), physical stresses on the cable within the stream, and the cable quality. These factors can be both spatially and temporally dependent and therefore need post-processing calibration to minimize their effect on the measurement data. Additional post-collection calibration increases the confidence in the internal reference coil's ability to maintain and capture accurate stream temperatures.

The post data collection calibration procedure involves the use of two known temperature profiles, preferably at the beginning and end of the cable length to account for gain. This technique is used to reduce or eliminate systematic and random error within the machine measurement outputs by isolating temperature offset and slope. The systematic error calibration procedure employs a method that simplifies the two known temperature segments by submerging a 15-20m coil of cable within an 'ice bath.' The ice bath consists of a cooler filled with ice with water added

to create a slurry at 0 °C. A single ice bath was placed at the upstream end of the stream in a shaded covering to reduce solar loading. Additionally, every morning and evening more ice was added to the slurry. Instead of placing another ice bath at the downstream boundary of the stream we spliced one of the internal fiber optics onto the other to create a loop for the light to travel. Splicing involves the bonding of two bare fibers through an electrical arc weld. All splicing in our study was carried out by a Fujiwara Fitel splicer. The circular path then allows for each trace to pass through the ice bath twice, expressing the slope of the trace and allowing us to calculate the slope calibration factor:

$$\hat{G} = \frac{(Ice_1 - Ice_2)}{L} \quad \text{Eq. 3}$$

where \hat{G} is the calibration gain factor [°C/m], Ice_1 and Ice_2 are the mean ice bath temperatures [°C], and L is the cable length [m]. The calculated gain calibration factor is then added to each corresponding section along the cable length.

One kind of random error, referred to as jitter, affects the entire cable and causes large jumps within the data with offsets as large as 2.3 °C (Huff, 2009). The jitter removal is done through a simple offset calculation:

$$\bar{T}(t) = T_{Raw}(t) - (T_{Raw, IceBath}(t) - T_{IceBath}(t)) \quad \text{Eq. 4}$$

where $\bar{T}(t)$ is the temperature offset in time, $T_{Raw}(t)$ is the DTS measured temperature at time (t), $T_{Raw, IceBath}(t)$ is the DTS temperature within the ice bath at time (t), and $T_{IceBath}(t)$ is the mean temperature of the ice bath at time (t).

5.3. *In or out of water identification*

Headwater streams, by definition, have an ephemeral nature to them at their most upslope portions and have a large range of flows associated. Additionally, the complex terrains that give rise to stream formation often result in step-pool sequences with substantial in-channel debris, creating some unique challenges for the application of DTS. For the WS07 stream, the most pressing issue concerns the question of determining where and when a cable is submerged in water or out of water.

Visual inspection of the data set has been the preferred method of isolating out of water cable (Huff, 2009; Collier, 2008; Westhoff et al., 2007). This method involves comparing the diurnal fluctuations of a stream temperature with the air temperature when the system experiences large diurnal variations. Sections of cable that are exposed to air have a visibly detectable difference in temperature to those that are in-stream. This method is effective in streams with low gradient with a small number of in-channel obstacles because relatively few out-of-water sections exist or that the out-of-water variability is minimal. Headwater streams do not meet these criteria and as a result both temporally and spatially numerous sections of cable are out of water. Much of the cable may be exposed to air in headwater streams making visual inspection time-consuming.

To address the problem in a more reliable and efficient way, we have developed an automated approach to identify out-of-water sections of DTS cable. We evaluated 4 methods against the verification dataset of in-water sections. The verification dataset was established through visual identification of each section of cable by comparing temperature traces from times of the maximum and minimum ambient air temperatures by hand. The out-of-water sections have distinct temperature differences comparative to those sections in-water, making visual identification an acceptable verification method for our automated approaches (Figure 4).

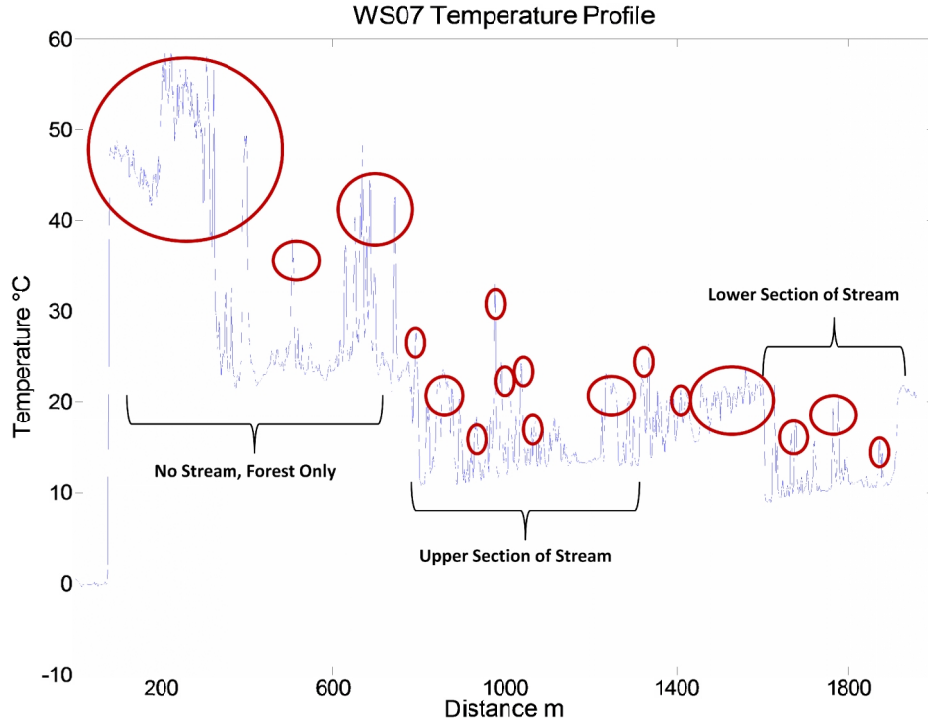


Figure 4: Time series of WS07 temperature profile. Red circles indicate examples of the out of water sections.

The 4 methods of in-water identification are defined as follows:

- 1) Method 1 compares the standard deviation of a known in-water section (STANDARD) during an 8 hour warming period (5am-1pm) to the standard deviation of all other cable locations during the same time period. If the difference in standard deviations is below a set threshold, the comparator is taken to be in-water.

$$\Omega_{STANDARD1} = \sigma \cdot (T(x_{STANDARD}, t)) = \sigma_{STANDARD} \quad \text{Eq. 5}$$

$$\Omega_{SECTION1} = \sigma \cdot (T(x_i, t_i)) = \sigma_{SECTION} \quad \text{Eq. 6}$$

where σ is the calculated standard deviation, $T(x_{STANDARD}, t)$ is the temperature profile for the known in-water section, and $T(x_i, t_i)$ is the temperature profile each section along the cable over the entire warming period.

2) Method 2 compares the rate of change during the same 8 hour period (5am-1pm) for the known in-water section and to all other locations. If the difference in rates is below a set threshold, the comparator is taken to be in-water.

$$\Omega_{STANDARD2} = \Delta T_{STANDARD} = \frac{|T_{\min} - T_{\max}|}{8hrs} \quad \text{Eq. 7}$$

$$\Omega_{STANDARD2} = \Delta T_{SECTION} = \frac{|T_{\min} - T_{\max}|}{8hrs} \quad \text{Eq. 8}$$

where $\Delta T_{STANDARD}$ and $\Delta T_{SECTION}$ are the calculated temperature rate of change over the eight hour warming period for the known in-water section and for each section along the cable, respectively.

3) Method 3 involves the same time period and preprocesses as method 2, and then compares the rate of change of each section versus the rate of change plus two standard deviations of the in-water sections.

$$\Omega_{STANDARD3} = \Delta T_{STANDARD} + 2\sigma(T(x_{STANDARD}, t)) \quad \text{Eq. 9}$$

$$\Omega_{SECTION3} = \Delta T_{SECTION} + 2\sigma(T(x_i, t_i)) \quad \text{Eq. 10}$$

4) Method 4 is formulated exactly the same as Eq.'s 9 and 10 except only one standard deviation is added.

$$\Omega_{STANDARD4} = \Delta T_{STANDARD} + \sigma(T(x_{STANDARD}, t)) \quad \text{Eq. 11}$$

$$\Omega_{SECTION4} = \Delta T_{SECTION} + \sigma(T(x_i, t_i)) \quad \text{Eq. 12}$$

For each of the four identification methods the first step, after general calibration and jitter removal steps, is to calculate a moving average of each section of

cable on an hour timescale. The 1-hour moving average eliminates some residual noise within the data. We then locate a section of cable that is known to be in-water to establish an in-water temperature fluctuation threshold that will be used as the standard we measure against to verify whether a section is in water or out.

The stream at WS07 has two distinct temperature regimes which we refer to as *Upper* and *Lower*. These are distinguished by being separated by a 250m section where the stream goes entirely subsurface, reemerging with a considerably lower and more constant temperature regime. We identified separate in-water sections in the *Upper* and *Lower* sections for the standard threshold calculations. The Upper section in-water standard had 31 distance measurement points at 32 times, while the Lower section in-water standard had 41 distance measurement points and the same 32 times. For every time increment, the entire length of in-water cable was averaged to obtain a single temperature measurement, i.e. averages of 32 data points per location in space. The standard deviation was then calculated for these sequential temperature measurements to obtain a single standard deviation for the time series, $\sigma_{STANDARD}$. For the individual sections outside of the in-water Standard the standard deviation calculation was simply the standard deviation of each section over the 8 hour time period of interest, $\sigma_{SECTION}$.

The calculation of $\Delta T_{STANDARD}$ was straightforward. We again took the average of every time increment so that we obtained 32 individual data points then determined the rate of change over the 8 hour period, $\Delta T_{STANDARD}$. The rate of change for each individual section outside of the in-water section was then found for the 8 hour time increment, $\Delta T_{SECTION}$.

Each method (Ω_i) was compared to the in-water standard ($\Omega_{STANDARDi}$). Any section where $\Omega_i > \Omega_{STANDARDi}$ was considered out-of-water and was thrown out of the matrix, while those where $\Omega_i < \Omega_{STANDARDi}$ were considered to be in-water. The 8 hour warming period from 5am-1pm was chosen because the thermal masses of ambient air compared to stream water at this time of day is small and therefore the stream change in temperature is muted and lagged compared to the surrounding air.

With any identification method there is a likelihood of errors in the identification process, typically defined as type I and type II errors. Type I errors are considered false positives, or specifically in our case the inclusion of cable sections as in-water sections that are in fact out-of water. Type II errors are the opposite or false negatives, i.e. the removal of in-water sections that were determined as out-of-water sections. To verify each method's ability to reduce type I and type II errors, we performed a check for veracity. At each section along the length of the cable during a warm summer period, we determined visually if the cable was in or out of water. Each section was noted and compared against the above procedure. Of the entire length of cable of 1155 sections we visually identified 379 sections as "in-water" leaving 32.8% of the potential temperature readings as valid stream temperatures.

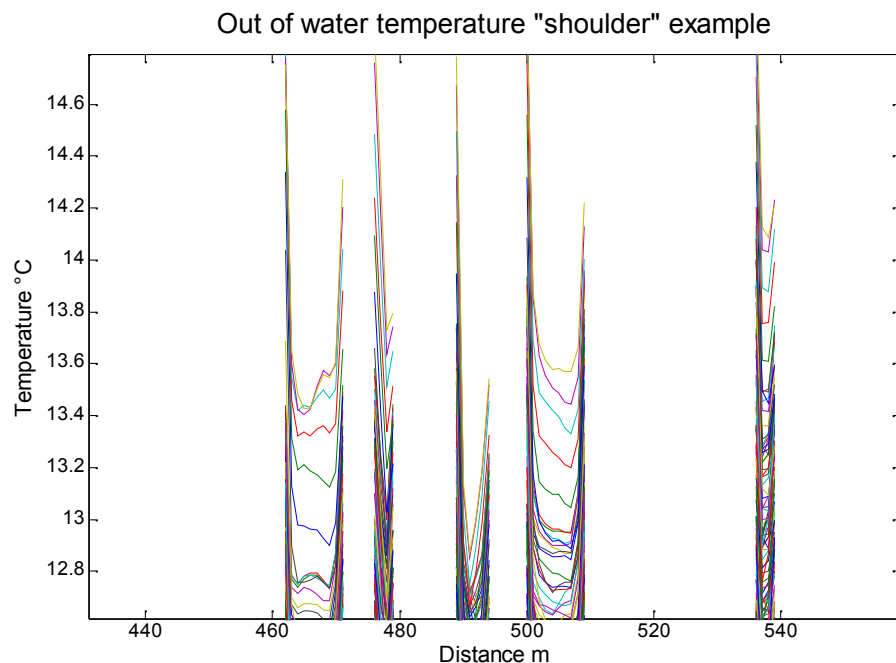


Figure 5: "Shoulder" example of headwater stream with DTS cable partially submerged. Each color represents a single temperature measurement in time.

Type I errors were overwhelmingly encountered at the 'shoulders' of temperature readings. Shoulders imply sections that were half in and half out of

water and exhibit reduced temperature fluctuations when compared against air temperatures while remaining below or equal to Ω_{STANDARD} . This problem persisted due to the cable having some portion within the water, enough to keep the temperature fluctuation of the section at a minimum but clearly above fully submerged sections (Figure 5), and also reflects the fact that DTS readings of the 5100 represent spatial averages of temperature over 1m, so reported temperatures for cable that was in water could reflect the out of water conditions within this distance of the transition.

Type II errors were also a common form of error and can be explained by the highly variable structure of the stream. Water within the stream channel in some places is only centimeters deep with relatively little vegetative shading and therefore high solar radiation loading causing their temperature rate of change to be much larger than the standard.

DTS cables are typically encased with a dark, UV-resistant polyethylene. Solar radiation penetrating shallow, low turbidity, and low velocity streams can contribute to heating up the cable increasing temperature measurement uncertainty. Incident solar radiation, incoming longwave radiation, conduction (from bed substrate), and outgoing longwave radiation from the cable are the primary energy balance components affecting the cable temperature. Neilson et al., (2010) demonstrated that dark DTS cables can exhibit significant temperature variation when compared to thermister measurements. In their study a measured difference of 0.007-0.13 °C in un-shaded Utah streams over a range of depths (0.05-0.8m) showed that cable placement and stream depth variability can have significant effects on measured temperature. This phenomenon contributes to the occurrence of type II errors where a cable that is completely submerged within water exhibits out of water behavior. Of course one may consider this to be a measurement that is not indicative of the true water temperature, and therefore its elimination could satisfy the objectives of the screening procedure despite the fact the cable is actually submerged in water.

We manually identified every in or out of water section along the entire length of the cable and used that matrix to compare our automated methods against to

determine each method's success rate. The results of the four identification methods above showed that method 3 had the most success. Method 1 correctly identified 69% of in-water cable sections, while method 2 had an identification success rate of 82%. Methods 3 and 4 employ a combination of the methods 1 and 2 and have a higher identification accuracy of 91% and 90%, respectively. Method 3 casts a wider net of variability tolerance in temperature measurements, 1.31 °C for the upper section and 0.49 °C for the lower section (2σ). Due to this type of stream where a high variability in form and structure occur, this method is seemingly preferred and was therefore employed in our study to determine the in-water portions of the cable. After eliminating out-of-water sections within the dataset we see that there are considerable portions of no-data (Figure 6).

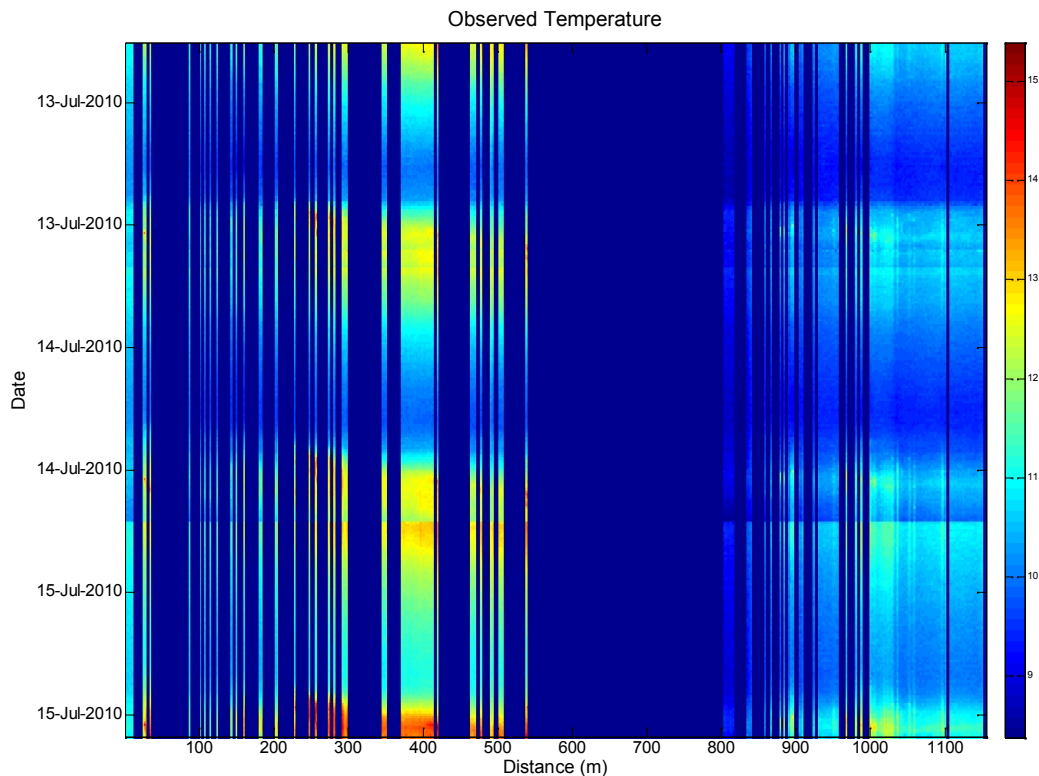


Figure 6: Dataset after out-of-water cable sections are eliminated. Dark blue areas are areas that were deemed to have been out of water.

5.4. *Measurement Uncertainty*

Stream structure variability and the physical obstacles present in headwater streams that make identification of cable submersion within the stream channel a challenge. These obstacles can increase output uncertainty by reducing the effectiveness of measurement detection. To be precise and confident in our stream temperature measurements we must account for these and any other forms of uncertainty. Temperature detection using the DTS method has uncertainty associated with it. We've identified three areas of uncertainty with DTS measurement: systematic machine specific measurement error, standard error associated with measurement precision, and measurement uncertainty relating cable placement within the stream.

The intrinsic temperature accuracy of DTS technology is reflected in the system is able to adequately measure stream temperature to a relative source. An internal temperature reference coil in the DTS is used to minimize measurement error. The SensorTran M4 5100 documentation lists an uncontrolled offset error associated with their internal reference coil, δ_{DTS} , of ± 1 °C (Table 2). However, we are able to reduce this error with our post-collection calibration using the ice-bath technique to account for offset.

To measure temperature precision for our deployment the standard measurement error was calculated during a time of constant temperature. This error is assumed to be space and time independent because of the changing external factors affecting the cable and therefore must be examined for a period when the cable had a known, constant temperature. The rationale is based on the central limit theorem, which states that measurement precision increases with the square root of the amount of independent data points included in an arithmetic average, i.e. the integration time of each DTS measurement:

$$\delta T(t) = \frac{\delta T'}{\sqrt{t}} \quad \text{Eq. 13}$$

where $\delta T(t)$ is the absolute measurement error at time t and $\delta T'$ [$^{\circ}\text{C}/\text{min}^{1/2}$] is the measurement precision at time (t). This states that the magnitude of the precision uncertainty of any given measurement decreases in proportion to the square root of the integration time (King et al., 1987). Absolute measurement error $\delta T(t)$ is calculated by:

$$\delta T(t) = \sigma_{IceBath}(t) \quad \text{Eq. 14}$$

where $\sigma_{IceBath}$ is the standard deviation of the raw ice bath. To calculate $\sigma_{IceBath}$, we used an ice bath to create this reference section of cable. The ice baths employed contained at least 20m of cable, and stayed at constant temperature of 0°C [$\pm 0.05^{\circ}\text{C}$] through thorough mixing of an ice and water slurry mix, and assuring that the ice extended all the way to the bottom of the slurry at all times. We used a 4 hour time series of 15 min readings and 20m of cable length resulting in 656 data points. Variation in the reported measurement of these 656 data points is considered to be indicative of the intrinsic uncertainty of the DTS readings and the constant temperature of the ice bath. The standard deviation was then calculated from the absolute measurement error and used as a measure of precision. For our deployment we calculated a measurement precision of $\delta T(t) = 0.15^{\circ}\text{C}$ using Eq. 14. Therefore with a 15min integration time interval we would expect $\delta T'$ to equal $0.46^{\circ}\text{C}/\text{min}^{1/2}$.

Finally, there is the temperature uncertainty resulting from the placement of the cable itself within the stream. Low flow periods and variable stream depths along the stream can cause temperature variations that do not represent the flux-weighted mean temperature. For instance, a cable sitting under 5cm of water is much more susceptible to temperature fluctuations from solar radiation directly than from a cable placed under 50cm of water. Being a high gradient stream with depths ranging from

5-25cm cable placement can have significant effect on the stream temperature measurement. Variable depths and widths, semi-rigid cable, in-stream debris, and rapidly changing flow regimes all contribute to the difficulty in having submerged cable in headwater catchment streams similar to WS07. To reduce these effects on measurement confidence we took multiple ‘known’ in-water sections and computed the measurement error for each in-water section, termed placement variability.

$$\delta_{Placement} = \frac{\sum(\sigma_1 + \sigma_2 + \sigma_3 + \dots \sigma_n)}{n} \quad \text{Eq. 15}$$

where $\delta_{Placement}$ is placement variability error (°C), and σ is the standard deviation of each cable section, 1, 2, 3, n. We selected 6 sections of cable that represent the range of measured water column depths under variable vegetation cover densities along the entire stream length. We based the evaluation on one hour of measurements taken during peak air temperatures, 1-2 pm, and calculated the standard deviation of each section over the submerged sections. It can be reasonable assumed that over the course of one hour stream temperature does not appreciably change so any variability within the measured output is a result of cable placement within the stream. From this we calculated the average standard deviation as 0.06 °C and used that value as what we call “cable placement uncertainty”, Table 3.

Table 3: One hour temperature measurement standard deviations of randomly selected sections of cable under differing canopy cover densities, as represented by their θ_{VTS} , and depth of water column.

Cable section MM	Average Depth [cm]	θ_{VTS}	Section σ [°C]
2-6	10	0.19	0.05
43-45	15	0.19	0.13
190-200	20	0.21	0.03
402-407	20	0.14	0.05
465-475	25	0.14	0.08
555-570	25	0.13	0.08

Mean: 0.06

Using Eq. 16 we determine a total uncertainty associated with DTS measurement of +/- 1.21 °C.

$$\delta_{Total} = \delta_{DTS} + \delta T + \delta_{Placement} \quad \text{Eq. 16}$$

However, because of our careful post-collection data calibration of calculating the temperature offset and gain using ice baths as our reference temperature, we can be confident that the machine error, δ_{DTS} , is no longer relevant. This resulted in $\delta_{Total} = +/- 0.21$ °C measurement uncertainty associated with the DTS. This understanding is critical for our purposes of determining lateral inflows at a point as well as temperature modeling.

5.5 Model Structure

Temperature simulation was performed using a modified HeatSource stream temperature model (Boyd and Kasper, 2003). The model is a physically based energy budget model that spatially and temporally constructs stream temperatures based on model inputs and pre-determined boundary conditions. The theory behind the model is one of a system of fully mixed reservoirs that respond to heat fluxes arising from advection, convection, radiation, and conduction. The original HeatSource model was adapted by Westhoff et al. (2007) to employ slightly preferred approximations for selected flux terms, and to place the model within the Matlab interface for ease of use and for easy integration of additional functions, i.e. groundwater seeps/sources and hyporheic zone inclusion. This adapted model has been successfully employed in numerous settings with a range of goals, including groundwater water detection in Luxembourg (Westhoff et al., 2007); land-use change implications in Switzerland (Roth et al., 2010); and a stream restoration project in Eastern Oregon (Huff, 2009).

The heat fluxes $\phi_{Radiation}$, $\phi_{Longwave}$, ϕ_{Latent} , $\phi_{Sensible}$, and $\phi_{Conduction}$ are incorporated within the model using energy balance Eq. 2. Each component of the energy balance

equation is outlined below. The most energetically important, component is net solar radiation, $\phi_{Radiation}$, which is broken down into direct and diffuse radiation.

$$\phi_{Radiation} = (1 - D_F) \cdot (\phi_{Direct} + \phi_{Diffuse}) \quad \text{Eq. 17}$$

$$\phi_{Direct} = C_s \cdot (1 - D_{Diffuse}) \cdot \phi_{Measured} \quad \text{Eq. 18}$$

$$\phi_{Diffuse} = D_{Diffuse} \cdot \phi_{Measured} \quad \text{Eq. 19}$$

Where ϕ_{Direct} and $\phi_{Diffuse}$ are measured direct solar radiation compensated for shadow effects (factor C_s [-]) and diffuse solar radiation [W/m^2], respectively. D_F is the fraction of solar radiation [-] which penetrates the stream column and goes to heating the streambed, $D_{Diffuse}$ is the fraction of solar energy which is diffuse, and $\phi_{Measured}$ is the solar radiation measured on-site by the Hi-15 Meteorological Station. The shadow effect for each grid cell, C_s factor, is calculated using TTools, an Arcview GIS extension developed by Boyd and Kasper (2003) to account for topographical and vegetative shading for 7 directions (e.g. NE, E, SE, S, SW, W, and NW). When the sun is below an individual grid cells topographical angle, $C_s = 0$ and when there is no shade obstruction, $C_s = 1$. $D_{Diffuse}$ is taken as 0.95 for the duration of the study. The on-site solar radiation measurement is assumed to accurately account for cloudiness and therefore no cloud variable was used in the calculation.

Net longwave radiation, $\phi_{Longwave}$, is the sum of three components:

$$\phi_{Longwave} = \phi_{Atm} + \phi_{Back} + \phi_{Land\ cover} \quad \text{Eq. 20}$$

where ϕ_{Atm} is the atmospheric longwave radiation to the stream, ϕ_{Back} is the back radiation from the stream to the environment, and $\phi_{Landcover}$ is the land cover radiation to the stream. Atmospheric longwave radiation is the “black-body” radiation that reflects the sum of emissions from the atmospheric air column and temperature of

deep space. Direct longwave radiation measurements are expensive and often are unavailable for catchment based studies and are therefore typically calculated using the Stefan-Boltzman law. It relates the emissivity of the atmosphere, an empirically derived constant, and air temperature through (Boderie and Dardengo, 2003):

$$\phi_{Atm} = 0.96 \cdot \varepsilon_{Atm} \cdot \theta_{VTS} \cdot \sigma_{SB} \cdot (T_{Air} + 273.2)^4 \quad \text{Eq. 21}$$

where ε_{Atm} is the atmospheric emissivity [-], θ_{VTS} is the view to sky coefficient [-], σ_{SB} is the Stefan-Boltzman constant [$5.67 \times 10^{-8} \text{ W/m}^2 \text{ }^\circ\text{C}^4$], and T_{Air} is the measured air temperature [$^\circ\text{C}$]. The parameter θ_{VTS} is a measure of vegetation cover density with a value of 1 representing a void of any stream vegetation cover. There are several ways of measuring or estimating the θ_{VTS} including, a series of spherical photographs taken upwards towards the canopy; a densitometer, or as a tuning parameter. The densitometer is a low technology concave mirror with a notched pattern on it that when holding it over the stream projects the canopy directly overhead onto the mirror. The user then counts the number of open notches on the mirror to gauge the effective canopy cover. For our study we initially took densitometer readings at 10 meter intervals up the stream length then spatially modified the θ_{VTS} as a tuning parameter in the calibration phase.

Emissivity is a measure of a material's ability, in this case the atmosphere, to emit energy by radiation (Brustsaert, 2007). It is a ratio of the energy emitted by that material and that of a perfect black body at the same temperature. Atmospheric emissivity varies according to cloud cover density and the concentration of gases that absorb and emit energy within the thermal infrared, i.e. 'greenhouse gases'.

$$\varepsilon_{Atm} = a \cdot \left(\frac{e_a}{T_{Air}} \right)^b \quad \text{Eq. 22}$$

Where e_a is the vapor pressure of air [hPa], a and b are empirical constants equal to 1.24 and 1/7, respectively. Eq. 22 is derived from Brutsaert (2007) and is valid for clear skies near sea level, with a standard error of 20-25 W/m² for cloudy conditions. Oregon summers are typically dry and with little cloud cover. The elevation effect on Eq. 22 was not taken into account.

Back radiation is the radiation emitted from the water to the atmosphere as “black-body” losses. This is the same principle as atmospheric longwave radiation and is therefore computed similarly using the Stefan-Boltzman law and calculated as (Boyd and Kasper, 2003):

$$\phi_{Back} = -0.96 \cdot \sigma_{SB} \cdot (T_{Stream} + 273.2)^4 \quad \text{Eq. 23}$$

All terrestrial bodies emit radiation, vegetation included. As with other longwave radiation, riparian vegetation absorbs solar radiation and reemits it as longwave radiation onto its surroundings, affecting stream temperature. Vegetation density and cover type has considerable effect on the amount of landcover radiation the stream receives. The land cover longwave radiation is computed as (Boyd and Kasper, 2003):

$$\phi_{Landcover} = 0.96 \cdot (1 - \theta_{VTS}) \cdot 0.96 \cdot \sigma_{SB} \cdot (T_{Air} + 273.2)^4 \quad \text{Eq. 24}$$

Turbulent fluxes of latent and sensible heat are difficult to directly measure in the best of cases, and in the setting of a small stream, are nearly impossible given the lack of uniform or consistent fetch conditions. High associated cost for their direct measurement prohibited us from using the standard eddy covariance method for measuring evaporation rates. Therefore to estimate the latent heat flux we employed the Penman equation for open water method as follows (Monteith, 1981):

$$\phi_{Latent} = -\rho_W \cdot L_E \cdot E \quad \text{Eq. 25}$$

$$L_E = 1000 \cdot (2501.4 + T_{Stream}) \quad \text{Eq. 26}$$

$$E = \frac{S \cdot \phi_r}{(\rho_w \cdot L_E \cdot (S + \gamma))} + \frac{(c_{Air} \cdot \rho_{Air} \cdot (e_s - e_a))}{(\rho_w \cdot L_E \cdot r_a \cdot (S + \gamma))} \quad \text{Eq. 27}$$

where ρ_w is the density of water [1000 g/cm³], L_E is the latent heat of evaporation [J/kg], E is the Penman open water evaporation rate [m/s], ϕ_r is the net (solar and longwave radiation) [W/m²], S is the saturated vapor pressure curve slope at a given air temperature [kPa/°C], γ is the psychrometric constant [kPa/°C], r_a is the aerodynamic resistance [s/m], and c_{Air} and ρ_{Air} are the specific heat capacity and density of air, respectively.

Sensible heat, the turbulent heat transfer between the air and water surface due to a temperature gradient is computed as:

$$\phi_{Sensible} = B_r \cdot \phi_{Latent} \quad \text{Eq. 28}$$

$$B_r = 6.1 \times 10^{-4} \cdot P_A \cdot \frac{(T_{Stream} - T_{Air})}{(e_s^W - e_a^W)} \quad \text{Eq. 29}$$

where B_r is the Bowen ratio [-], P_A is the adiabatic atmospheric pressure [kPa], T is the water temperature [°C], and e_s^W and e_a^W are the saturated and actual vapor pressure [kPa] at the water-air interface. The Bowen ratio is a method that represents the proportion of available energy at the air-water interface that is passed to the atmosphere as latent heat or sensible heat.

The substrate over which the stream flows affects the stream temperature by heat transfer resulting from the temperature difference between the water column and the bed material. Bed conduction is typically modeled as a two layered system; one that is affected by surrounding heat fluxes and has a diel fluctuation, and a second

deeper layer that is assumed to be constant in temperature and consistent with the groundwater temperature.

$$\phi_{Net} = \phi_{Solar} \cdot \left(\frac{D_F}{1 - D_F} \right) - \phi_{Conduction} + \phi_{Alluvium} \quad \text{Eq. 30}$$

$$\phi_{Conduction} = -K_{Soil} \cdot \frac{(T - T_{Soil})}{d_{Soil}} \quad \text{Eq. 31}$$

$$\phi_{Alluvium} = -K_{Soil} \cdot \frac{(T_{Soil} - T_{Alluvium})}{d_{Soil}} \quad \text{Eq. 32}$$

Where K_{Soil} is the volumetric weighted thermal conductivity [J/m s °C] of the soil, $T_{Alluvium}$ is the temperature of the deeper alluvium, T_{Soil} and d_{Soil} are the temperature [°C] and depth of soil [m]. These equations assume that the stream bed is saturated.

5.6 Model calibration parameters and sensitivity analysis

After model inputs were measured or calculated, the model was then calibrated by optimizing the parameters θ_{VTS} , D_{Fo} , and $T_{Alluvium}$ by minimizing the root means squared error (RMSE) against the observed DTS temperature output. RMSE is calculated by:

$$RMSE = \sqrt{\frac{\sum (T_{Sim} - T_{Obs})_i^2}{n}} \quad \text{Eq. 33}$$

where T_{sim} is the simulated temperature at i^{th} time interval, T_{obs} is the observed temperature, and n is the total number of observations.

The parameters represent the total amount of incoming shortwave radiation available at the water surface (D_{Fo}), the view to sky coefficient (θ_{VTS}), and the

temperature of the deeper alluvium ($T_{Alluvium}$), which we assume is constant at a depth of 0.2 m. After calibrating, $T_{Alluvium}$ was taken to be the same for the whole stream (9 °C), while θ_{VTS} differed for each combination of stream conditions, and D_{F0} varied with vegetation cover and water depth. D_F is determined by use of a Beer's law exponential extinction equation and varies with water depth. The solar radiation intensity reaching the streambed decreases exponentially with the measured stream depth profiles as follows:

$$D_F = D_{F0} \cdot e^{-\alpha d} \quad \text{Eq. 34}$$

where D_F is the fraction of incoming shortwave radiation that penetrates the water column and goes to heating the substrate depending on the vegetation cover type as determined by the calibration procedure, α is the extinction coefficient where a mean value for water was used (0.05m^{-1}) (Mobley, 1994), and d is stream depth (m). In this study α is considered a constant that reflects the water's ability to absorb and diffuse light, for example, turbidity of the stream. The D_F and θ_{VTS} parameters appear in the energy balance equations 17, 24, 30, and 34 and their calibrated values used in the model are shown in Table 4.

Table 4: Post-Model Calibration Model
Parameter Values for D_F , θ_{VTS} :

Distance Downstream	D_F [-]	θ_{VTS} [-]
0 – 125m	0.6	0.19
125 – 245m	0.8	0.21
250 – 400m	-	-
400 – 495m	0.8	0.14
495 – 590m	0.9	0.13

5.7. Tracer study

Determination of stream flow at a point can be done in a variety of ways, e.g. weirs, interpolation of direct measurement with flow meters, and dilution gauging.

Dilution gauging involves the addition of a non-reactive chemical at a known mass-loading rate into the stream, and the measurement of its rate of dilution by means of mass balance. A common stream tracer is NaCl, because of its low cost, ready availability, non-toxic nature, and ease of measurement with electrical conductivity probes. The potential for harmful effects to the stream ecosystem are minimal due to the low concentrations that are typically used and the duration of the experiments. The dilution gauging technique is widely employed in stream reaches that are difficult to measure with flow meters because of non-uniformity sections common in high order mountain streams renders direct measurement unreliable and difficult to implement. Additionally, dilution gauging can give spatially distributed flow measurements establishing areas of subsurface connectivity within the system.

There are two types of salt dilution methods commonly employed: constant rate, and slug injection. The slug injection method is ideal for mountain streams with high flow up to $10 \text{ m}^3/\text{s}$ with steep gradient and turbulent flow (Moore, 2004b). This approach involves injecting a known volume of salt solution at a near instantaneous slug into the stream. The salt solution mixes rapidly with the stream water through advection and dispersion. At a desired location downstream the electrical conductivity (EC) of the stream is measured with an EC meter. As the salt cloud passes the EC meter a steep rising limb is produced. As the salt wave passes the meter the peak begins to retreat and the stream slowly returns to background salt concentration levels. The time required for the peak of the salt wave to move through the EC meter is inversely dependent on the mean velocity of the streamflow, while the duration of the salt wave will depend on how variable the velocity profiles are within the stream (Moore, 2004b).

The constant rate method is better suited for small streams, less than 2m wetted channels, with low flow characteristics. A salt solution is injected at a constant rate into the stream and will become mixed at some distance below the injection point through turbulent flow. Once steady state conditions are met, where the relative stream salt concentration is in equilibrium, stream discharge can be computed.

Because stream relative salt concentration is linearly related to EC measurements, k , this method allows for simple calculations of stream flow through the following (Moore, 2004a):

$$Q = \left(\frac{q}{k} \right) \cdot (EC_{SS} - EC_{BG}) \quad \text{Eq. 35}$$

where Q is stream flow [m^3/s], q is the injection rate [m^3/s], EC_{SS} is the steady state EC measurement, and EC_{BG} is the background EC measurement of the stream (prior to injection). The linear relationship between stream salt concentration and EC, k , is derived through a predetermined calibration curve of the instrument.

An alternative approach to determining discharge from the salt dilution method is through mass integration. This method uses the trapezoidal rule to calculate stream salt concentration which approximates the area under the curve between two points in time as a trapezoid. Individual areas are summed to find the total area under the curve.

$$Area = \frac{L}{2} \cdot (p_H + w_H) \quad \text{Eq. 36}$$

where L is base length and p_H and w_H are the salt concentrations at each of the trapezoid vertical sides. Once the area is found for each segment, they are summed to find the entire area under the curve. This method requires at least one discharge measurement. Discharge at location i , Q_i , is then equal to:

$$Q_i = \left(\frac{Area_q}{Area_i} \right) \cdot q \quad \text{Eq. 37}$$

where $Area_q$ is the area at the location of the discharge measurement, $Area_i$ is the location of interest, and q is the measured discharge [m^3/s]. To evaluate surface and

groundwater interactions within the WS07 stream a constant rate injection NaCl⁻ dilution tracer approach was employed. The salt tracer injection was performed on a 550m section of the stream that is characterized by riffle-step –pools and with an average slope of 17 degrees. The study took place from July 7-9th 2008 with near constant flow conditions and moderate temperatures. A 220 L solution containing 13.5kg of table salt (NaCl⁻) as a conservative tracer was injected into the thalweg using a battery powered peristaltic pump at a rate of 100 mL/min. The duration of the injection was 49hrs and was monitored continuously for Cl⁻ concentration at two locations using 2 YSI multisonde conductivity probes. Additional salt concentration measurements were taken at pre-determined sampling points at 15min intervals for the first 2 hours after injection and every hour thereafter throughout the duration of the study. The pre-determined sampling points were located every 10 meters along the stream length directly upstream of where the stream went subsurface, 50m downstream from the injection point, and after it had reemerged, 300m downstream from the injection point.

An additional study to collocate groundwater interactions using the DTS method was carried out from 12-15th July 2010. The purpose was to not only to collocate seeps and sources but to also determine the interannual variability of groundwater inflow quantity.. DTS technology enables spatial and temporal temperature measurements ideal for stream temperature variation detection. To determine groundwater interaction, termed lateral inflow, within the stream we employed a combined mass and energy balance approach (Selker et al., 2006b). This method uses the principles of conservation of both mass and heat by measuring upstream and downstream temperature of two stream temperature profiles (1 and 2) with a known stream discharge to determine lateral inflow quantity by combining the mass balance equation and the energy balance equation for stream temperatures:

Mass Balance: $Q_D = Q_U + Q_L$ Eq. 38

Energy Balance: $T_D Q_D = T_U Q_U + T_L Q_L$ Eq. 39

$$Q_L = Q_D \cdot \frac{(T_{D1} - T_{U2} - T_{D1} + T_{U1})}{(T_{U1} - T_{U2})}$$
 Eq. 40

where Q is discharge [m³/s], T is the water temperature [°C] and the subscripts *D*, *U* and *L* are downstream, upstream and lateral inflow, respectively. The assumptions of this equation state that the downstream temperature and lateral flow temperatures are fully mixed. Results will be artificially high if thorough mixing does not occur. Additionally, the longitudinal increments between measurements must be such that there is no appreciable energy exchange from the upstream to the downstream measurement sites. Measurements of temperature used in Eq. 40 were averaged over a 4 hour period and lateral inflows were calculated as well as total discharge along the longitudinal profile of the stream.

5.8. *Bedrock topography and soil property methods*

5.8.1. *Knocking pole*

Subsurface bedrock delineation was determined by use of the dynamic cone penetrometer (Herrick and Jones, 2002), hereafter called ‘knocking pole’. Knocking poles are designed to determine the resistance force of soil by supplying a known amount of kinetic energy to the knocking pole, causing it to move through the soil at various increments depending on the kinetic energy applied to the knocking pole, the geometry of the tip, and the soil penetration resistance. Other soil resistance penetrometers rely on constant velocity, which is subject to operator variability, and thus hinders repeatability, and the device is mechanically controlled by a fixed hammer mass and drop heights. The apparatus consists of 0.5m length sections of stainless galvanized steel with one section having an attached strike plate (anvil) welded to the shaft. Additional sections can be added for various depths. The shaft continues through the plate and is used to guide a 5 kg stainless steel slide hammer

The knocking pole is operated by placing the pole vertical with the cone base level with the soil surface to minimize starting depth. The hammer is then lifted to a mark 0.5m above the plate and drop under the force of gravity alone creating a constant work term. The depth of the knocking pole is marked down and this operation is then repeated until the 'depth of refusal' is reached. Depth of refusal is defined as when the knocking pole does not penetrate more than 5cm after 20 or more knocks and is assumed to be bedrock or a layer of undeveloped saprolite which acts as an impeding layer. This method measures the depth of penetration into the soil per blow of the hammer.

The knocking pole method can be used to calculate a soil penetration resistance averaged across the distance the cone moves through the soil after each hammer blow. Soil penetration resistance is defined as the force applied to the knocking pole by the soil (Herrick and Jones, 2002). Resistance is calculated as the work done by the soil to stop the force of the knocking pole divided by the distance the knocking pole moves into the soil:

$$R_s = \frac{W_s}{P_D} \quad \text{Eq. 41}$$

where R_s is the measured soil resistance in Newtons [N], W_s is the work done by the soil in Joules [J], and P_D is the distance the knocking pole moves into the soil in meters [m]. Work done by the soil is calculated as the change in the kinetic energy of the knocking pole. The kinetic energy of the knocking pole after it is stopped by the soil is zero and therefore the work done by the soil is equal to the kinetic energy transferred to the cone from the knocking pole (Herrick and Jones, 2002). This method assumes that all the kinetic energy from the falling hammer is transferred to the cone. Work done is calculated as follows:

$$W_s = 0.5 \cdot m \cdot v^2 \quad \text{Eq. 42}$$

where v is the hammer falling velocity [m/s] and m is the hammer mass [kg].

5.8.2. Soil cores, soil particle distribution, and hydraulic conductivity methods

In addition to the knocking pole method to determine bedrock topography and soil resistance we also determined saturated hydraulic conductivity and particle size distributions on selected soil samples. At select locations within WS07 we took soil core and bulk soil samples at various depths using standard soil core methods (Day, 1965). From these samples we determined soil particle distributions using a hydrometer and saturated hydraulic conductivity using the constant head method.

Hydrometer analysis

A hydrometer measures the displacement of a bulb in fluid. The amount of displacement is the buoyancy of the bulb and buoyancy is proportional to the density of the fluid. As more particles are in solution, the density increases and the bulb displaces less fluid. Particles falling within solution are subject to the force of gravity (downward) and the drag force (frictional force upward). This drag force is derived using Stoke's Law, which states that the frictional force exerted on spherical objects with very small Reynolds number (e.g. very small particles) in a continuous viscous fluid is proportional to the viscosity of the fluid, the falling velocity, and the radius of the sphere. When the drag force equals the gravitational force then terminal velocity is reached, i.e. settling velocity. The time it takes for sediments in solution then can be used to determine the particle size distribution.

Each sample was preconditioned by grinding a 50 g bulk soil sample using a mortar and pestle to eliminate large aggregates of soil. An additional 50 g sample was oven dried at 105 °C for 24 hours. Once the sample was thoroughly ground up, the sample was put through a #48 sieve with the addition of water and vigorously shaking the sample. The coarse grains (>2mm) were collected, dried and weighed. The

remaining sample was added to a 1 L solution containing 100mL of dissolved Calgon for the purpose of breaking down any residual soil clots. Each hydrometer was calibrated by taking the temperature of the 1 L Calgon solution and a reading the hydrometer at the upper edge of the meniscus. The solution and sample were then mixed and the temperature was noted. The hydrometer was then placed within the solution. Time and hydrometer measurements were at the beginning, 60 sec, and 180 sec. Then the hydrometer was rinsed and lowered back into solution where additional hydrometer readings were taken at 10 min, 30 min, 90 min, and 270 min rinsing the bulb after each reading. These time increments correspond to settling time of soil particles with diameters of 0.0456mm, 0.0269mm, 0.0149mm, 0.0087mm, 0.0050mm, and 0.0029mm.

Each hydrometer reading (R) is recorded along with the time. The concentration of suspension [g/L] equals:

$$c = R - R_L \quad \text{Eq. 43}$$

and the summation percentage calculated by:

$$P = \frac{c}{(c_o)} \cdot \frac{1}{100} \quad \text{Eq. 44}$$

where c_o is the oven-dry weight of the sample [g/L]. The particle size is then calculated for length in microns in the following way:

$$X = \frac{\theta}{\sqrt{t}} \quad \text{Eq. 45}$$

where θ is the corresponding value for R from table 43-7 in the Methods of Soil Analysis Handbook (Day, 1965).

Saturated hydraulic conductivity analysis

Understanding the rate of movement of water through soil is fundamental in hydrological applications. The physical properties of soil control the resistance to flow, along with the pressure gradient (head). This resistance to flow is termed the hydraulic conductivity of a soil. It is a measurement of the soils ability to transmit flow or conversely the resistance to flow. Dating back to Henri Darcy's famous studies on the public water fountains in Dijon, France in 1856 has saturated hydraulic conductivity been measured. Darcy's Law is the principle physical relationship equation used to describe the flow of water through porous media.

$$Q = K_{SAT} \cdot A \cdot \frac{\Delta H}{\Delta L} \quad \text{Eq. 46}$$

where Q is the volumetric flow rate [m³/s], A is the cross-sectional area of the column [m²], H is the hydraulic gradient or head [m], L is the length of the column [m], and K_{SAT} is the permeability of the media [m/s].

The procedure involves preparing each soil core by saturating it overnight in a CaSO₄ solution. After set-up of a tempe cell water is set in motion through the set-up to relieve all air bubbles from the system. Any residual air will disrupt the procedure due to the pressure differences. Once the system is purged and ready water is sent through the system. Once steady state within the system is achieved, time, outflow, and the change in pressure head are all measured. From these measurements K_{SAT} can be calculated using equation 46 above. Summary statistics and sampling locations and depth for the hydrometer analysis and for saturated hydraulic conductivities are given in Table 6 and 7.

5.9. Metrological stations and other measurements

Atmospheric measurements were continuously recorded at a meteorological station located within the watershed (Figure 2) as part of the National Science Foundation funded Long Term Ecological Research (LTER) network. Measurements

included relative humidity, air temperature, vapor pressure, and wind (both magnitude and direction) all at 1.5m and 4.5 m heights above ground, incoming solar radiation, barometric pressure, soil temperature (0.1m, 0.2m, 0.5m, 1m). All measurements are taken 15 minute intervals. Additionally, stream gauge heights and precipitation inputs, including both rain and snow depth, were measured.

6. Results

6.1. Tracer results

Results from the salt tracer study which took place July 7th - July 9th, 2008 provide a representation of surface and subsurface water interactions within WS07. Hourly specific conductivity (SC) longitudinal profiles were measured at 10m increments along the entire stream length. Specific conductance is a temperature corrected measurement of the electrical conductivity of the stream. Figure 7 gives the breakthrough curves (BTC) at each wetted flag (1-9 at the lower reach, 20-27 at the upper reach, with flag numbers going from biggest to smallest as you move down stream) for the entire length of the study (Figure 21).

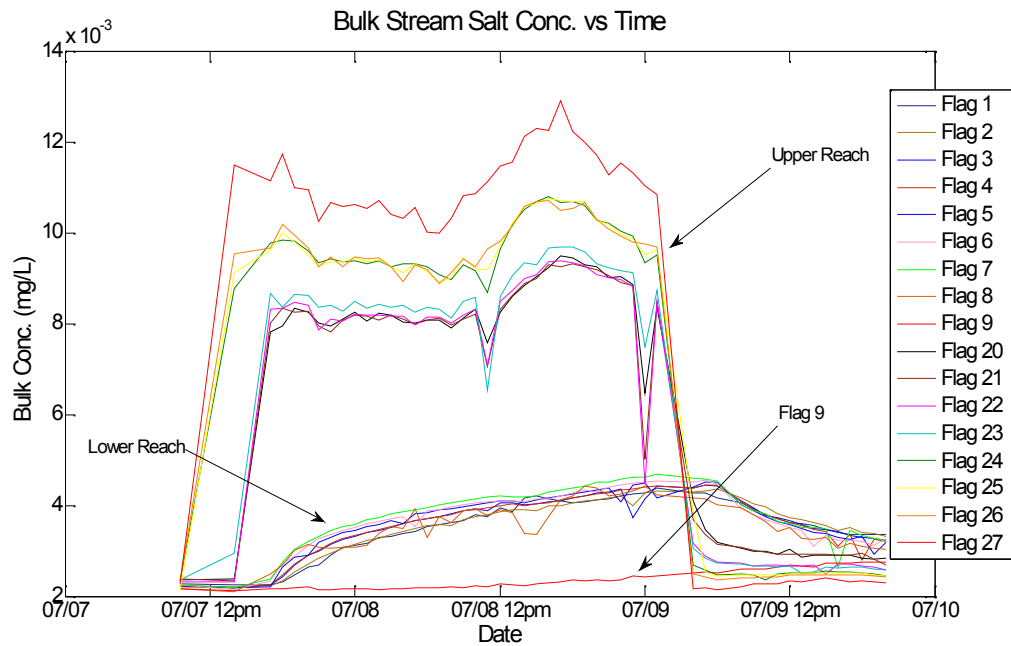


Figure 7: Bulk Salt Concentration for each location along the stream length.

These curves begin with the background stream SC. Once the salt injection is begun, each flag increases in SC to a plateau. Flag 27 has the largest plateau value, 222.9 $\mu\text{S}/\text{cm}$. The dips in SC in the upper reach correspond to points when the pump broke down and stopped the salt concentration injection. The pump malfunctions occurred on July 8 at 11:00am and again on July 9 at midnight. The dip was not recorded at flag 27 because we fixed the pump just upstream of the flag as soon as we recognized the pump failure. The pump was turned off on July 9 at 3:00am. After turning off the pump, SC levels throughout the stream began to return to background concentration levels. The differences between the time to reach plateau levels and return to background levels reflect increasing groundwater inputs and variable subsurface water flow paths.

Figure 7 shows two noteworthy groundwater inputs into the upper stream reach. Lower specific conductivity measurements are a result of lateral inflow, which dilutes the salt concentration at the measurement location. Groundwater inputs can be clearly seen between flags 27 and 26 and flags 24 and 23. After flag 20, the stream goes completely subsurface until the stream reappears at flags 9 and 8. Less distinguishable inputs exist between nearly all flags, accounting for the slight translations in SC data for all times.

Using conservation of mass and the known discharge to be 1.3 l/s at flag 23 where the stream gauge was located, the discharge at each flag was calculated using Equations 35. Flag 27 had a discharge of 0.993 l/s and flag 1 had a discharge of 2.541 l/s. The total increase in discharge was 1.548 l/s. The three substantial groundwater inflows between flags 27 and 26, 24 and 23, and 20 and 8 were calculated to have inputs of 0.135, 0.113, and 1.127 l/s, respectively. Figure 8 plots the change in total discharge [l/s] at each flag using two different methods: the blue diamonds are the discharge computed from the plateau values (Eq. 37) and the green stars are the discharge values computed using trapezoidal integration (Eq. 35).

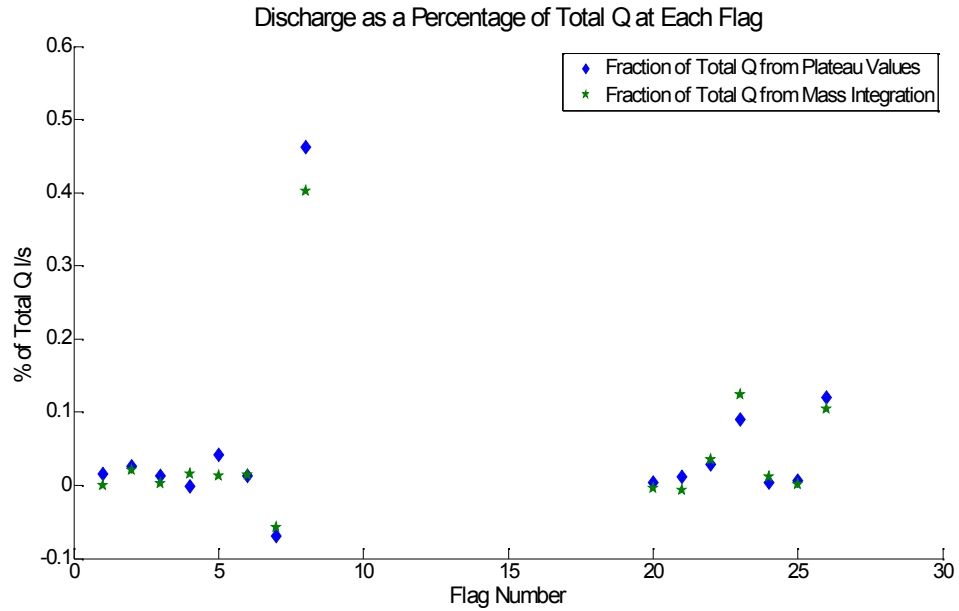


Figure 8: Change as percent of total discharge at each location (l/s) along the stream.

The discrepancy in the discharge values using equations 35 and 37 in the lower reach is due to the fact that the tracer application was not sufficient in duration to achieve steady state. Figure 9 presents a linear increase of discharge through both sections of the stream reach. Flag 8 appears to be an anomaly to the stream’s overall surface and subsurface flow pattern. It is located at an isolated pool that functions as a spring with minimal connection to the subsurface flowpaths of the upper portion of the stream. Its high calculated discharge is primarily caused by the diluted salt concentration signal due to the minimum connection with the upper section.

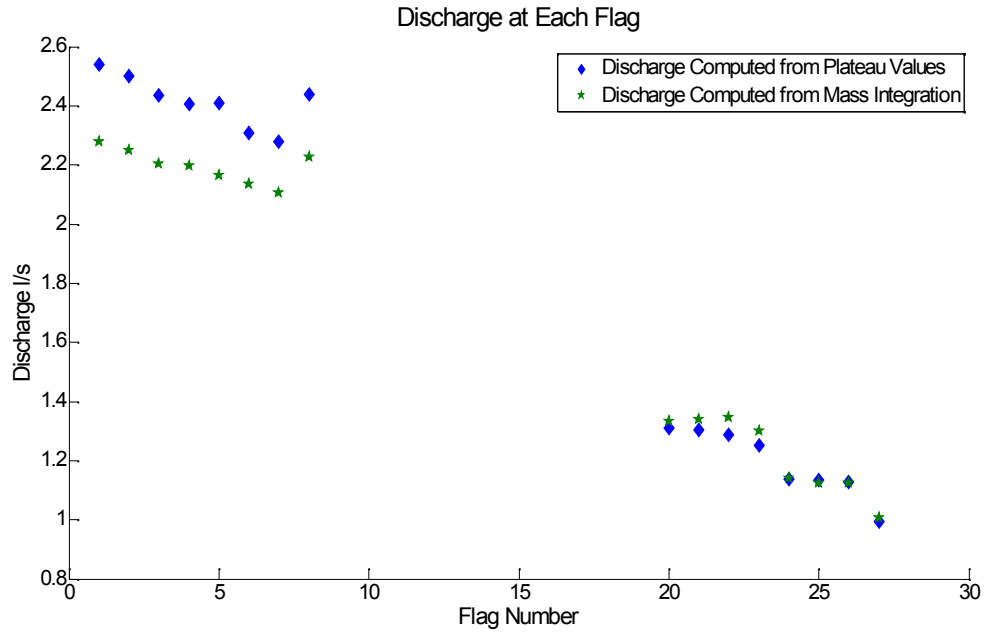


Figure 9: Calculated discharge for each location (l/s) along the stream.

The stream was dry above it until flag 20, and dry below it until flag 9. The bulk concentration at flag 9 took approximately 17 hours to get above background levels and never reached a steady state bulk concentration. This suggests that flag 9 has a different flow path than flags 1-8. While it does have some connection to the upper stream due to its apparent rise in SC, its connection is considerably slower suggesting that it is mixing with a large subterranean groundwater system that is significantly diluting the signal, thus we left discharge calculations of flag 9 out of our results.

This anomaly challenges the assumption that allows us to use conservation of mass to compute the lower reach stream discharges. The flag 9 data in Figure 7 shows the existence of multiple subsurface flow paths, so it is entirely possible that the lower reach has lower bulk concentration not only because of large volumes of groundwater inputs that were not part of the upper section surface water, but also because of subsurface flow paths that when the stream goes subsurface circumvent the study reach entirely, discharging the salt at a location further downstream.

Figure 9 demonstrates the importance of reaching steady state conditions when trying to calculate discharge. The lower reach discharge, flags 1-8, calculated from

plateau salt concentrations deviates considerably from the mass integration calculations. There seems to be a systematic shift in discharge in the lower section where none exists in the upper section. Looking at Figure 7 we see that the lower section, although quite close, probably never reached steady state and therefore the plateau values used in Eq. 37 are actually lower than what would have been the case resulting in increased discharge calculations.

Along with the bulk concentration data, temperature readings were also taken during the hourly profiles. Figure 10 relates temperature as a function of time and flag. This figure shows that there is a diurnal stream temperature fluctuation, with the exception of flag 9. The maximum temperatures occur at 2:00pm and the minimum temperatures occur at 7:00am. There is a substantial decrease in stream temperature between flags 20 and 9. The subsurface flow between the upper and lower reach provides a buffer for the stream temperature. The hyporheic exchange buffer is an important component during the summer when the stream has lower flow and is receiving higher energy inputs, e.g. short and longwave radiation and sensible and latent heat fluxes. This groundwater temperature buffer is clearly seen at flag 9. Flag 9 has a muted diurnal cycle that stays relatively constant at 7.5 °C. This provides greater evidence of a large groundwater composition in Flag 9.

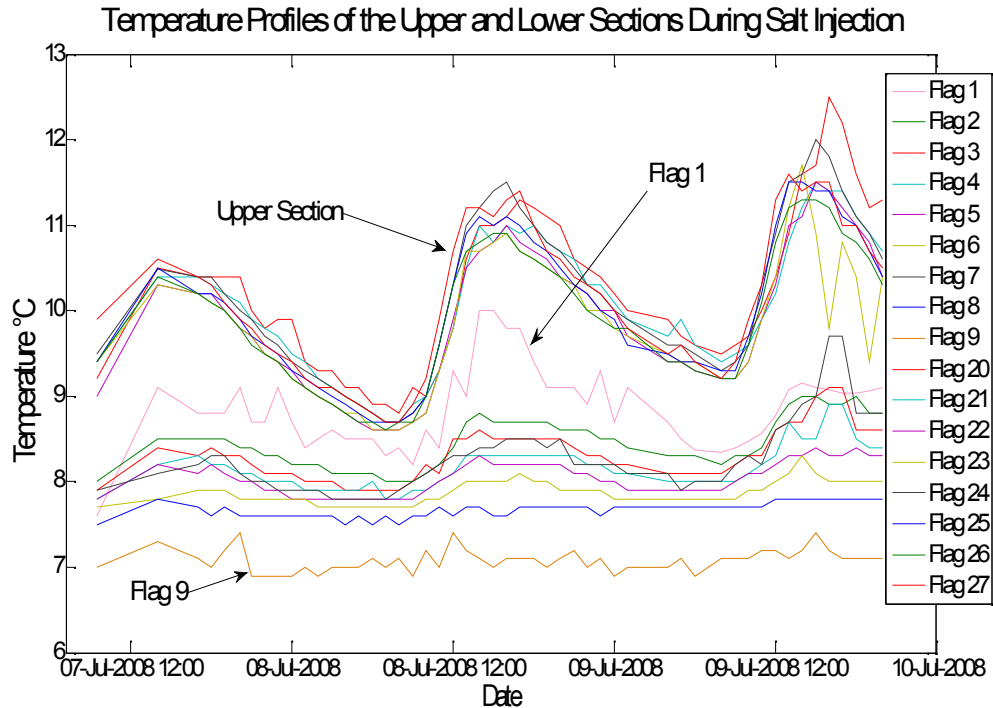


Figure 10: Longitudinal profile of WS07 stream of specific conductance vs. time vs. stream temperature.

During the period closest resembling plateau salt concentrations, there is a small diurnal SC cycle that corresponds with the stream temperature diurnal cycle. The trough of the temperature cycle coincides with a trough in specific conductivity. This says that more groundwater is being input into the stream lowering the temperature and diluting the salt concentration. The opposite occurs during the crest of the temperature and SC diurnal cycle. This pattern highlights a relationship between ground and surface water and the diurnal evapotranspiration pattern of the surrounding vegetation.

6.2. DTS results

WS07 stream temperature signature is a result of the energy fluxes it experiences and the environment in which it lies. The upper section of the stream (from MM 0-538) is characterized by having higher temperatures, both maximum and

average, than the lower section (MM 803-1155) (Figure 11). The relative lack of vegetation density plays a role in higher radiation exposure but also contributing to the reduction in temperature is that the water emerging at the lower section has travelled through the subsurface and mixed with a vast store of groundwater. Water reemerging at the lower section spring (MM 803 and corresponding to flag 9 above) exhibits muted temperature diurnal fluctuations compared to the upper section further suggesting that this spring is largely influenced by groundwater (Figure 12). Maximum and minimum DTS measured temperatures over the course of the study were 14.68 °C and 8.43 °C, respectively, Figure 12.

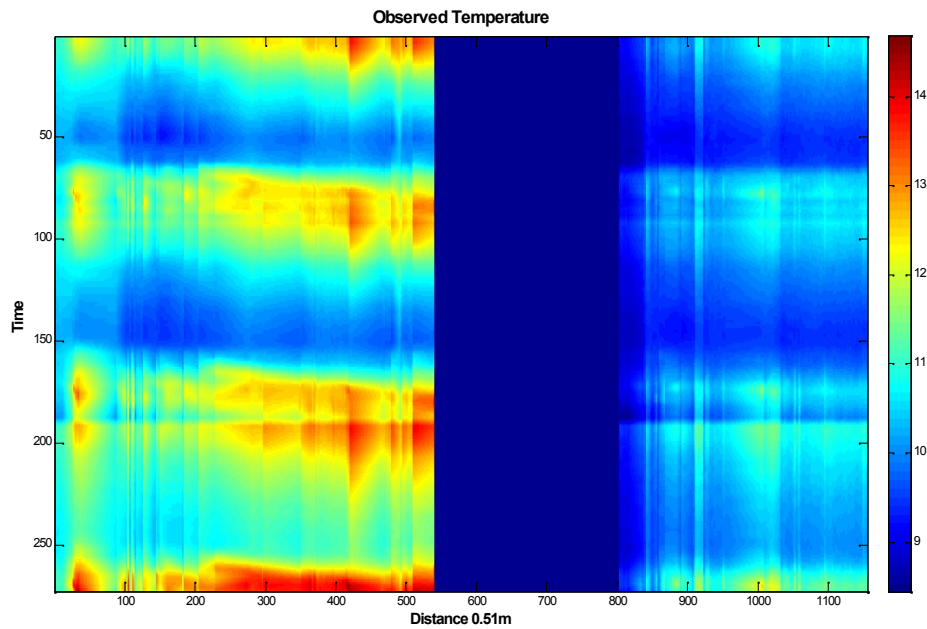


Figure 11: DTS measured stream temperature. Dark blue represents the subsurface portion of the stream. Vertical striations are result of linearly interpolated measurements of in water sections. The pronounced horizontal striation during day three is from a power supply outage.

The WS07 stream was modeled to run for the two distinct sections with model output for the subsurface portion suppressed. The subsurface section had no energy balance inputs calculations that were readily available so we modeled the two

sections separately, each having initial conditions inputs from the observed DTS measurements. These two sections, apart from their temperature regime differences, have distinctly different riparian zones. The upper section of stream flows through a young forest stand that was clear cut in 1974 and 75-80% thinned in 1998. The thinning harvest was not minimal and much of the forest was harvested. The remaining forest cover is immature Douglas Fir, young Red Alder, and various shrubs that provide little radiative shading. Conversely, the lower section flows through a mature old growth Douglas Fir and Cedar forest and a dense overstory that keeps the stream well shaded. These distinct canopy differences also play a major role in the stream temperature profiles for each section of stream.

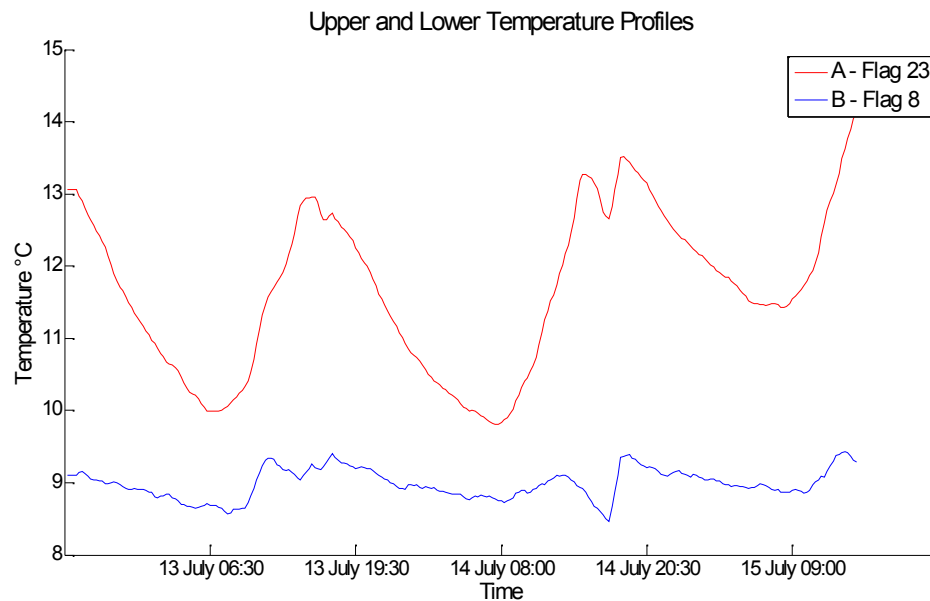


Figure 12: Temperature profiles of the points along the stream where A) Flag 23 and B) Flag 8.

Model analysis involved calculating the RMSE of the simulated stream temperature against the observed stream temperatures for each section, upper and lower. The calibrated the energy balance model performed well in representing the system, RMSE = 0.38 °C and 0.32 °C for the upper and lower sections respectively as compared to the observed DTS measurements (Figure 11 and 13).

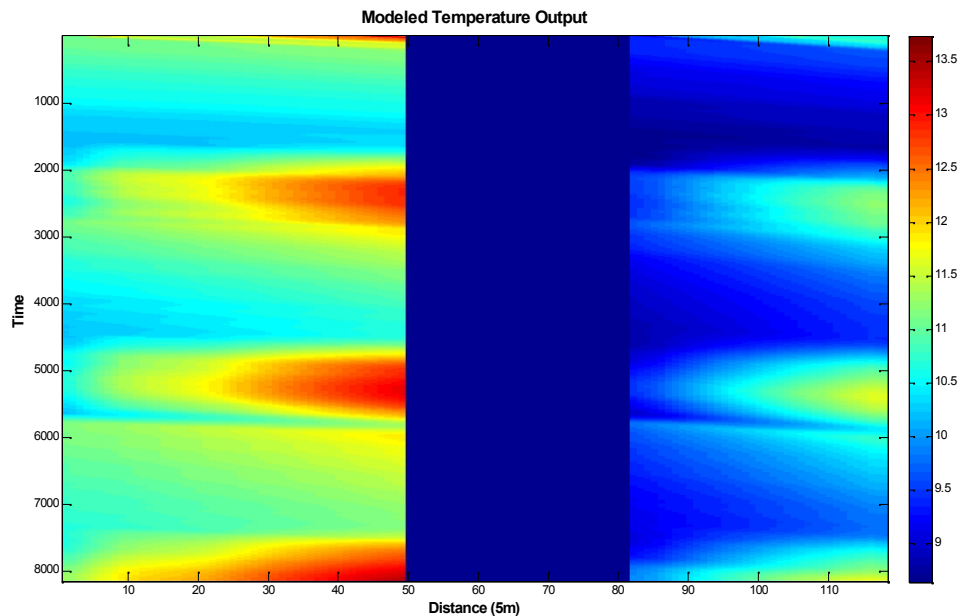


Figure 13: Simulated model temperature in space and time (x and y axis). Dark blue section represents the subsurface portion of the stream.

To evaluate stream temperature response from energy flux, we calculated four summary statistics related to temperature extremes: mean peak, mean minimum, absolute maximum, and absolute minimum. We examined the modeled temperature differences using these metrics for the two stream sections. Mean peak temperatures were calculated from a 2-hr time period, 1:00-3:00 p.m. for mean maximum and 4:30-6:30 a.m. for mean minimum. Spatially, the mean temperatures were calculated at the downstream boundary of the stream for each section. At the downstream boundary of each section, the mean peak in-stream temperature should be an indicator of the stream temperature response to the integrated upstream influences on the stream. As expected, the upper section showed a consistently higher mean peak average, 13.40 °C compared to 10.90 °C for the lower section (Figure 14 and 15). Absolute temperature maxima and minima are a relevant statistic because while many in-stream biota are susceptible to daily mean temperature changes, others are at risk to extreme temperature variation. Mean minimum temperatures can expose effects

of substrate on stream temperatures and subsurface mixing. Mean stream velocities of 0.05 m/s and 0.02 m/s for the upper and lower sections result in hydraulic residence times of 1.98 h and 2.30 h, respectively. The two sections show differences in average minimum temperature of 1.15 °C (10.8 and 9.6 °C). The higher minimum temperature in the upper section is a result of the lack of mature vegetation cover and leads to radiative cooling from reducing the amount of longwave radiation into the stream and allows slightly higher evaporation rates. Consideration of the energy balance affecting the stream is useful in understanding these results (Table 7).

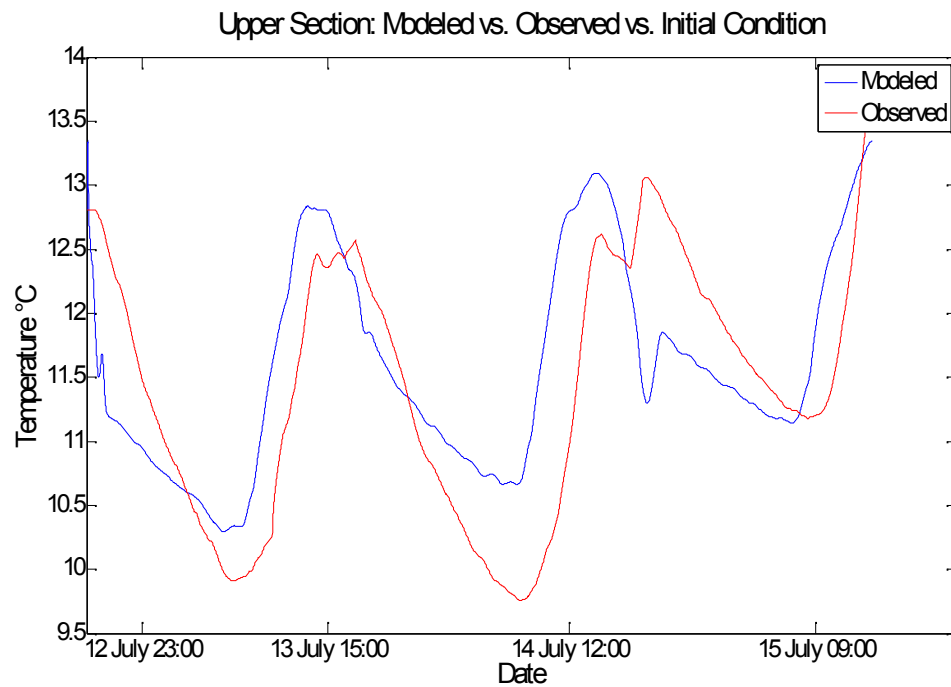


Figure 14: Upper section at downstream boundary modeled versus observed temperature [°C] profile for the study duration.

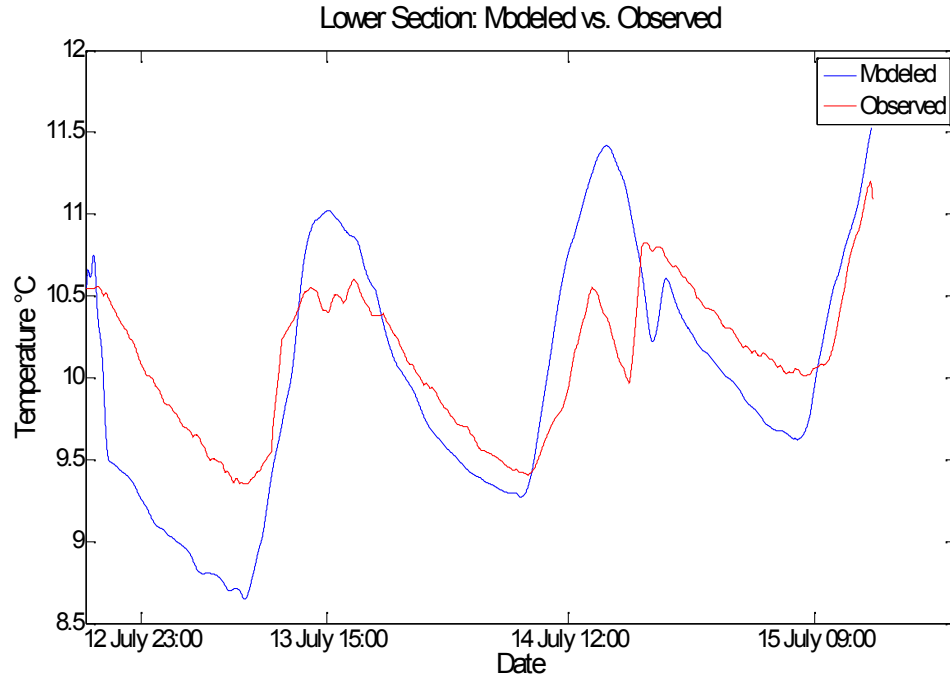


Figure 15: Lower section at downstream boundary modeled versus observed temperature [°C] profile for the study duration.

Table 5: Average Energy Balance Components for both Sections of River, computed for 1:00-3:00 pm during July 13th-15th 2010.

Energy Balance Component	Energy (W/m ²)	
	Calibrated Upper	Calibrated Lower
Direct incoming solar radiation (SW_D)	189	59
Land cover longwave radiation (LWR_L)	352	382
Surface emitted longwave radiation (LW_S)	-360	-351
Atmospheric longwave radiation (LW_{ATM})	81	54
Bed conduction (COND)	34	50
Latent heat flux	-77	-51
Sensible heat flux	83	67
Total	302	210

Surface-emitted longwave radiation and land cover longwave radiation loads are not altered in any considerable way for our simulations and, in general, cancel each other out. Relative differences in the evaporative flux relate to the total radiation load and the gradient of relative humidity, and therefore, we see the highest evaporation

within the upper section while the lower section has considerably less evaporative heat loss.

Direct incoming solar radiation is the driving component in the energy balance, which along with considerable lateral inflows cause the temperature differences in these two sections. For example, the lower section receives only 30% of the incident solar radiation than the upper section. This is primarily a result of the solar shadow effect as the lower section is located in a topographically pronounced hollow. This enforces the notion that solar radiation is a first-order control to stream heating. Mature forest cover has influence on various microclimate forcings that drive the energy balance, such as wind speeds, humidity, and air temperature. However these were not explicitly measured under the canopy of the lower section.

Surface-emitted longwave (outgoing) and land cover longwave (incoming) fluxes essentially offset each other, leaving direct incoming solar radiation to account for the majority of total radiation load into the upper section of the stream. This makes it the most significant term within the energy balance in the upper section and subsequently the term that provides the most in-stream temperature change. For the lower section solar radiation plays a lesser role in the energy balance. Atmospheric longwave radiation and bed conduction become significant terms in the energy balance. The atmospheric longwave radiation is a function of both the θ_{VTS} coefficient and the air temperature. Considering that the meteorological measurements for the lower section were made at the Hi-15 met station that is located in a clearing void of vegetation cover, it is logical to expect that the measured peak air temperatures would be higher than under the old growth canopy. For this reason we expect the atmospheric longwave radiation term to be higher than expected as the Stephen-Boltzman equation is primarily controlled by T_{Air}^4 (Eq. 24).

6.3 *DTS and Salt Tracer Lateral Inflow Comparison*

Using heat as a tracer is a useful for identification and quantification of hydrological interactions both in the subsurface and in surface water (Constantz 2008;

Stonestrom and Constantz 2003; Selker et al., 2006b; Westhoff et al., 2007). Groundwater inflows change the temperature regime of a stream depending on their temperature difference, spatial frequency, and volumetric discharge. Headwater streams experience high amounts of lateral inflows and are intimately linked with the subsurface system due to their upland location within basin. The salt tracer experiment that took place on July 7th-9th, 2008 verified this statement showing that the WS07 stream gained 0.32 l/s over a 50m stretch before it went subsurface, or 24% of the measured streamflow. Upon resurfacing streamflow was shown to be 2.4 l/s, almost double the flow in the upper section. The lateral inflows in WS07 represent a significant portion of discharge which is congruent with a similar finding by McGuire et al., (2004). McGuire et al. demonstrated that sustained lateral flow from a trenched hillslope seepage face in a headwater stream at the H.J. Andrews Experimental Forest contributed upwards to 15% of volumetric stream discharge from highly localized lateral sources during fall dry conditions.

Considering the dynamic nature of lateral inflows to headwater systems we sought to investigate the spatial distribution of groundwater discharge from 2 different time periods under similar flow conditions. We compared lateral inflows found during the 2008 salt dilution study to those found using DTS in the summer of 2010. In July 2010 DTS measured temperatures of the WS07 stream were used to identify and quantify lateral inflows contributing to stream discharge using Eq. 40. Measured stream discharges at the gauge house between the two studies were nearly identical during the experiments, 1.35 l/s in 2008 and 1.4 l/s in 2010. From this we assume similar groundwater table position. We calculated lateral inflow amounts at the same locations as the salt tracer experiment using two methods, mass integration and salt concentration at steady state values (Figure 16).

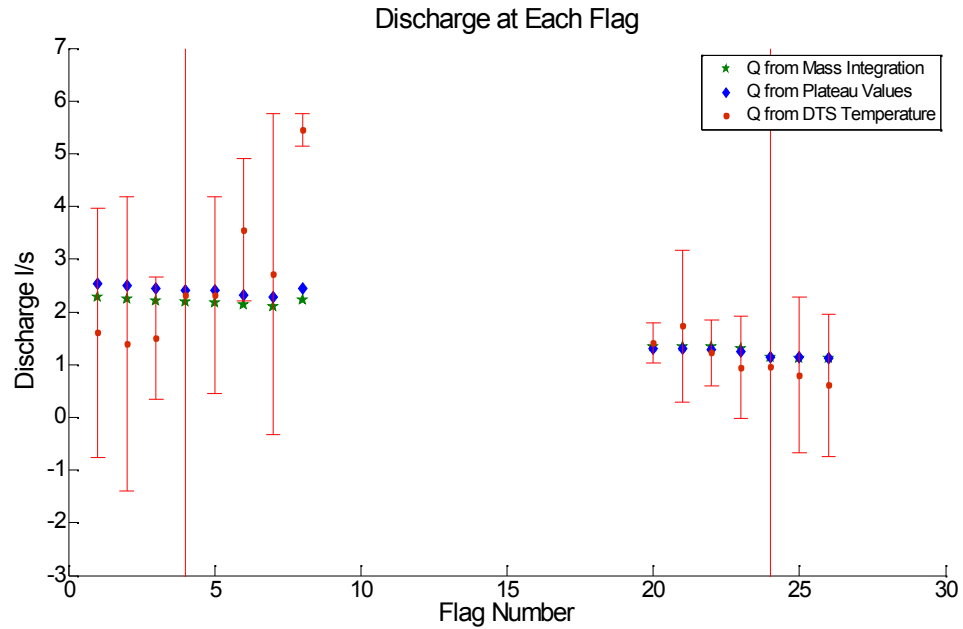


Figure 16: Discharge calculated from salt dilution and DTS measurements.

Both salt dilution methods, mass integration and plateau salt concentration at steady state conditions, had similar discharge patterns of a gaining stream in both the upper and lower sections. However, when using heat as a tracer, lateral inflows in the lower section showed significant deviation from the salt tracer methods. In fact the latter method depicts a losing stream, after the large initial spring inflow upon reemergence, losing over 4 l/s over the 80m stretch.

The lower section, as previously noted, has a muted temperature signal as compared to the upper section from reduced solar loading and the groundwater spring at the reemergence point. The reduction in calculated discharge can be attributed to the stream losing heat as it moves downstream or through losing volume to the subsurface (Eq. 40). Recalling Poole and Berman (2001), we know that changes in stream temperature are proportional to heat energy and volume. From the reemergence point, flag 8, to 80m downstream to flag 1 the average peak stream temperature rises from 9.08 °C to 10.57 °C.

In examining Eq. 40, lateral inflow amount is inversely proportional to the temperature difference between the two chosen profiles in the upstream direction. If

those two temperature profiles are similar at a given point then discharge will increase. From Figure 16 we see the largest subsurface lateral water migration into and out of the stream channel largely takes place in the lower section, primarily near the reemergence point. These points also are sections where we measured the least amount of diurnal temperature fluctuation.

Errorbars in Figure 16 are calculated based on propagation of uncertainties using a variation of the sums/differences and products/quotients provisional rule (Taylor, 1982).

$$\left(\frac{\delta q}{q}\right) = \sqrt{\left(\frac{\delta f}{f}\right)^2 + \left(\frac{\delta g}{g}\right)^2} \quad \text{Eq. 47}$$

$$\delta f = \sqrt{(\delta T_{D2})^2 + (\delta T_{U2})^2 + (\delta T_{D1})^2 + (\delta T_{U1})^2} \quad \text{Eq. 48}$$

$$f = T_{D2} - T_{U2} - T_{D1} + T_{U1} \quad \text{Eq. 49}$$

$$\delta g = \sqrt{(\delta T_{U1})^2 + (\delta T_{U2})^2} \quad \text{Eq. 50}$$

$$g = T_{U1} - T_{U2} \quad \text{Eq. 51}$$

where δ for each temperature measurement, T, is equal to the total measurement uncertainty as found through Eq. 16, 0.21 °C. The propagation of uncertainty associated with DTS measurements when determining lateral inflows is substantial, especially in low flow headwater streams such as WS07. Examining Figure 16 further we see that the confidence level in our estimations of discharge vary widely, on average +/- 3.8 l/s (this excludes the high uncertainty value found for flag 4 and 24). Considering that the stream itself varies 0.9-2.3 l/s in discharge measurement uncertainty associated with DTS can mask small lateral inflows. This should be taken

into consideration when using this method of groundwater seep/source identification, especially low volume streams.

At two locations along the stream we see large uncertainties that range from +/- 10-15 l/s, at flag 4 and 24. This is a result of the relative change between the two temperature profiles used at these particular locations in Eq. 51 and similarly in the propagation of error equation, Eq. 47. One assumption of Eq. 51 is that the temperature profiles used in determining the energy balance between upstream and downstream must be sufficiently different to register meaningful volumetric change. Additionally, comparison of the upstream and downstream sections must be located sufficiently close to each other so as to avoid any change in stream temperature by outside energy inputs. By looking at the inverse temperature measurements of the numerator ($1/f$) and the denominator ($1/g$) we see that the large uncertainties associated with discharge measurements become apparent (Figure 17).

The large inverse temperature differences apparent in Figure 17 at flag 4 and 24 for $1/f$ match the large uncertainties in Figure 16.

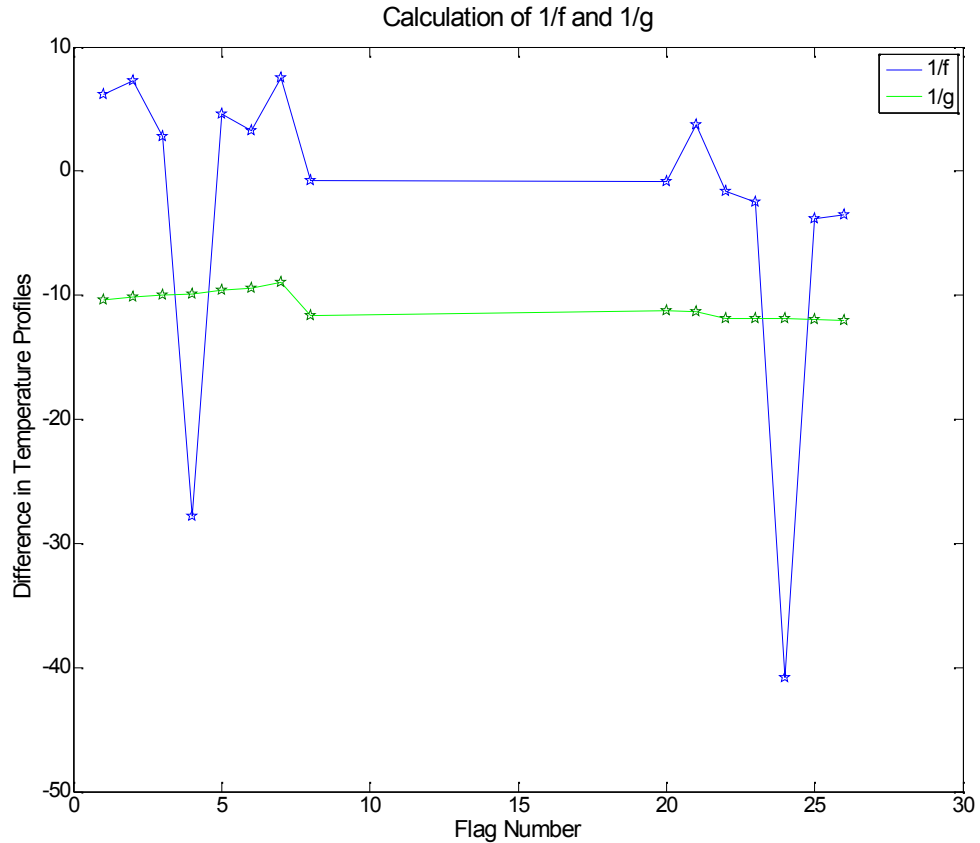


Figure 17: Calculations of 1/f and 1/g in equations 49 and 51.

If the temperature profiles of the upstream and downstream sections have similar temperature profiles then large uncertainties in lateral inflow quantification will arise. This is largely due to the assumption that groundwater is of a different temperature than that of the stream. In our case we can safely assume this is the case as the average yearly air temperature at WS07 is well below the daily maximums used in our calculations. Because no change in stream temperature existed between the upstream and downstream flags of 4 and 24, we assume that no groundwater source is located there. At flag 4, for example, the difference between the two profiles for the upstream section and the downstream section are 0.91 and 0.87, the difference between the two is only 0.04 °C. This results in a very small f in Eq. 48 which forces $(\delta f/f)^2$ to be large.

6.4. Soil characterization

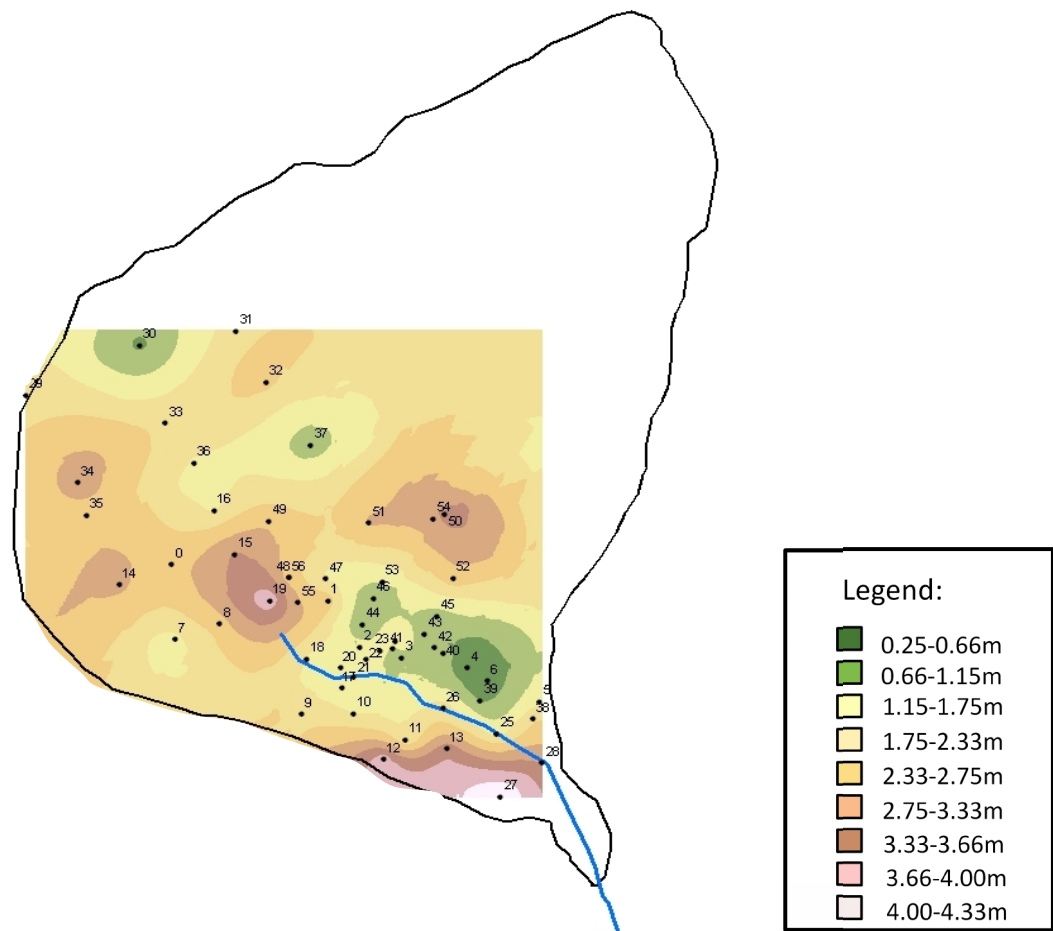


Figure 18: WS07 knocking pole depth to bedrock surface layer at each location.

Knocking pole field experiments were carried out to obtain the depth to bedrock and total catchment soil volume (Table A1 gives complete knocking pole data). Figure 18 shows the point measurements of depth to bedrock with a kriged GIS layer overlain. Kriging of point data linearly interpolates point data to all intermediate points within a predetermined spatial scale. The underlying assumption with kriging is that deterministic variables have a linearly defined spatial correlation with truly random variables (Royle et. al., 1981; Davis, 1986). This means that variables nearby a measured point are more likely to resemble that point than variables at greater distance. Soil depths ranged from 0.24m to 4.13m. Depth to bedrock showed a slight

negative correlation with slope angle (Figure 19) but the strength of the R^2 value (0.12) suggests that local topography is not a primary control on soil depth. A negative correlation is expected as gravity driven colluvial transport of soil migrates towards the valley bottoms. The entire catchment area is 21 ha and using an average soil depth found by the knocking pole experiments of 1.92m, we calculate that the total soil volume is 403,000 m³.

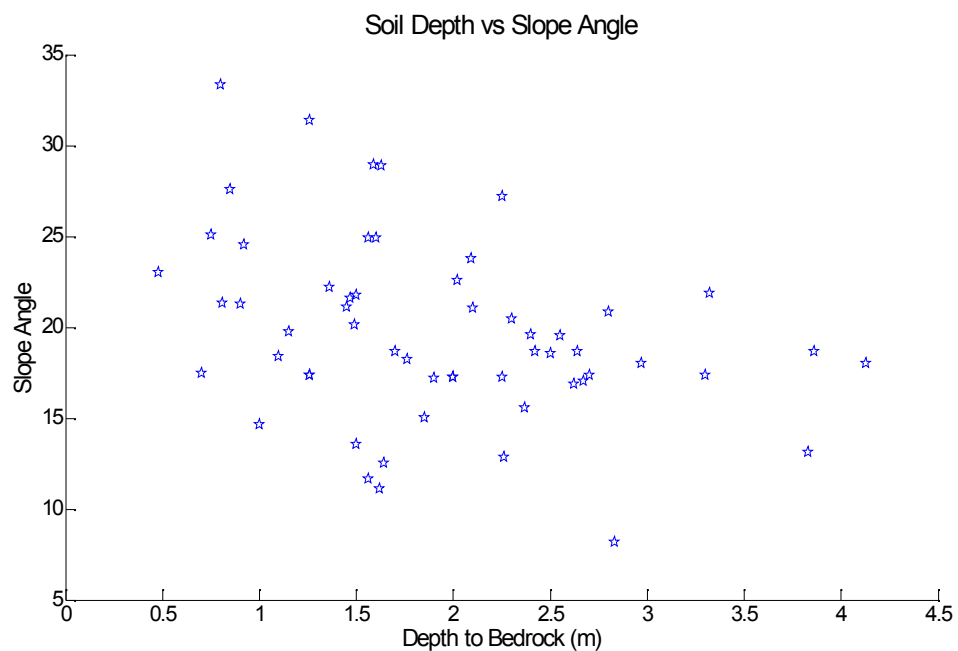


Figure 19: WS07 Slope angle versus depth to bedrock at each knocking pole location.

Determination of soil depths is an essential component for water balance calculations and allows one to begin to understand water storage and recharge potential within a catchment. However depths alone are not sufficient. With this in mind we examined bulk soil samples for the particle distribution and soil cores for hydraulic conductivity measurements. These soil properties are important metrics in subsurface transport processes. Particle size analysis of the 13 measured soil samples indicate that the less than >2mm soil particle fraction is made up of primarily fine silts with a clay fraction ranging from 1.4 % in the upper profile to 6.5 % at depth (Table 6).

This silty loam soil has a reddish brown color and a grainy texture with 30% sand content. Saturated hydraulic conductivity analysis showed that K_{SAT} decreased with depth from 9×10^{-5} m/s at 30 cm depth to 2×10^{-7} m/s at 1m depth (Table 7), demonstrating a decrease in permeability with depth.

Table 6: Average Soil Particle Size Distribution (%) from the 11 sample sites.

Depth	Particle Size Distribution (mm)							n
	> 0.2950	0.0456	0.0269	0.0149	0.0087	0.0050	0.0029	
0-40 cm	37.6 %	22.8 %	16.6 %	10.9 %	11.5 %	8.7 %	5.8 %	3
40-75 cm	35.4 %	18.8 %	14.1 %	9.4 %	8.5 %	2.9 %	2.9 %	3
75-115 cm	29.1 %	20.9 %	10.4 %	5.2 %	9.5 %	4.6 %	5.7 %	4
115-150 cm	20.3 %	13.7 %	8.4 %	7.2 %	8.7 %	5.8 %	6.5 %	3

Table 7: K_{SAT} values (m/s) from soil cores at various depths using the constant head method.

Depth	K_{SAT} (m/s)	n
0-30 cm	9.06E-05	4
30-70 cm	8.63E-05	5
70-100 cm	2.09E-07	2

Hydraulic conductivity below the surface has been described using a power law decay function (Rupp and Selker, 2005) and with an exponential decay function (Beven 1984).

$$K_{SAT} = K_0 \cdot e^{-FZ} \quad \text{Eq. 54}$$

where K is hydraulic conductivity [m/s], Z is depth below the surface [m], and F is a coefficient [-]. WS07 soils are not exempt from this functional relationship of decrease in permeabilities with depth. Beven (1982b and 1984), argued that in areas where rainfall rates are sufficient enough to saturate the surface layer, infiltration to depth is controlled by the largest continuous pore size. These large pore spaces can be

naturally formed through preferential flowpaths occurring when instabilities arise during the seasonal drying of soils, the fining of soils, and compaction, as well as from a result of biotic interaction within the subsurface, i.e. root channels and burrowing biota. With increasing depth these processes are minimized in some logical way (Beven, 1984).

Infiltration of precipitation and run-off processes within a catchment have a rich history within hydrology (Philip, 1957; Horton, 1942; Hewlett and Hibbert, 1967; Dunn and Black, 1972). From the extensive research devoted to this endeavor many models that aim to replicate fluid transport in the subsurface have been formulated. The Green and Ampt approach to compute infiltration is commonly employed to test hypotheses of the effect non-homogenous soil characteristics on infiltration with depth (Beven, 1984; Selker et al., 1999a). The Green and Ampt approach models vertical and horizontal infiltration as taking place due to gravitational and capillary forces, with a sharp wetting front separating the saturated soil column from the initially dry soil (Selker et al., 1999b). It is assumed that no preferential fingered flow exists and that the drivers of infiltration are the force of gravity acting on the water and the suction produced by wetting front. The model gives rise to a prediction of the depth of infiltration flux in time under constant head infiltration is given by (Selker et al., 1999b):

$$q = \sqrt{\frac{(K \cdot h_f \cdot n)}{2t}} = \frac{S \cdot \sqrt{t}}{2} \quad \text{Eq. 52}$$

where q the infiltration flux, K is the hydraulic conductivity, h_f water entry pressure within the soil, t is time, and n is soil porosity. S is the sorptivity term, and relates to the capacity of a medium to adsorb (or desorb) water by capillarity (Philip, 1957) that is dependent on the medium and is equal to:

$$S = \sqrt{(2n \cdot K \cdot h_f)} = \sqrt{C \cdot r} \quad \text{Eq. 53}$$

The term C encompasses all of the aforementioned specific soil properties to give a single soil characteristic term. Equation 52 shows that infiltration flux into the soil decreases proportionally with the square root of time. By having an understanding of how the soils compact and fine at depth, one can begin to understand how the infiltrating flux will change with depth and time. Equation 53 shows us that infiltration flux into finer soils (smaller pore radii) decreases by the square root of the characteristic soil radius. We've shown above that infiltration flux decreases with the square root of r . However, this is in contrast to how pore size affects hydraulic conductivity as the underlying control on K in that it decreases with r^2 . This is an important relationship because it allows us to better understand subsurface flow based on the simple characteristic pore size radius.

Similarly to the exponential decrease of K_{SAT} with depth, soil resistance, was also found to exhibit this same relationship. As defined by Eq. 41, soil resistance was calculated for each knocking pole location. The soil resistance increased exponentially in almost all cases. Figure 20 depicts some examples that show the exponential pattern. Low soil resistance in the first 100 cm of the soil profile is demonstrated in all cases. As the depth increases and the knocking pole passes into more compact soils, the resistance increases sharply. This is congruent to hydraulic conductivity decrease with depth. The uniformity of the soils resistance is remarkably similar for all cases until we get close to the bedrock. As the bedrock nears the soils become much more resistant and more compact. This suggests that infiltration should be near uniform in the upper sections of the soil and that the limiting K_{SAT} values for groundwater recharge will be found near the soil bedrock interface.

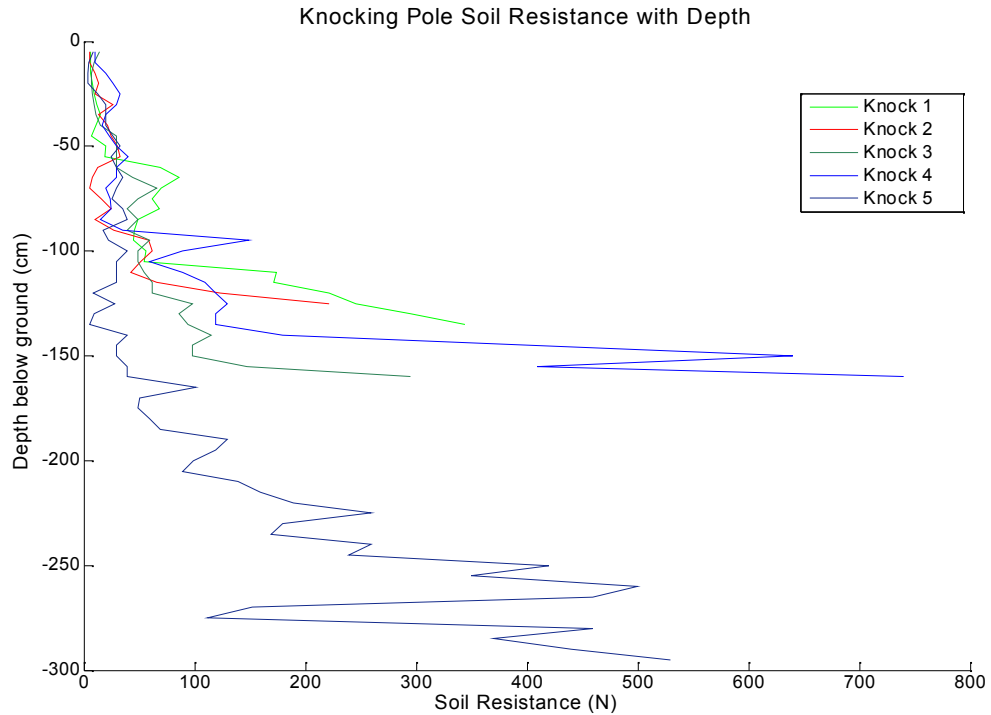


Figure 20: Soil Resistance for 5 knocking pole site locations. An expressed exponential increase of resistance with depth is present.

Knocking pole measurements not only give soil resistance but they also delineate the bedrock topography. Bedrock topography can be important to hydraulic routing as the sharp change in permeability between overlaying soil matrix and the less permeable bedrock surface often induces lateral flow. Where local depressions exist at the soil-bedrock surface, subsurface perching of groundwater can occur. If the capacities of these depressions are exceeded water can move laterally along the soil bedrock interface surface, a process defined as ‘fill and spill’ by Tromp-van Meerveld et al., (2006). The fill and spill hypothesis is used to explain subsurface stormflow threshold behavior that Tromp-van Meerveld et al., (2006) observed at the Panola Mountain Research Watershed in Georgia.

Figure 18 gives the bedrock topography of WS07 in relation to the soil depths as found through the knocking pole measurements. The areas in green in Figure 18 shows a large region of sustained shallow soil depths where the mean depth is 0.63m,

with a range of 0.25-1.13m (Table A1). The 16 knocking pole measurements represent a small area of total catchment area but could be the most hydraulically active area for groundwater recharge in the entire catchment. We may thus consider the hypothesis that hydraulic conductivity is a primary control on infiltration and therefore net groundwater recharge within a catchment. Infiltration rates must exceed the lowest permeability value in order to achieve recharge. With a soil porosity of 0.3 and total soil volume of 403,000 m³, we calculate a total potential available storage volume of approximately 121,000 m³ for the catchment.

To determine the amount of groundwater infiltration potential consider, for example, that our lowest reported K_{SAT} value of 2×10^{-7} m/s or approximately 2 cm/day is the threshold value for recharge. With this hydraulic conductivity we can calculate daily average infiltrated flux reaching the soil/bedrock interface of approximately 2×10^{-2} m/day or 2 cm/day. Extending over the entire catchment area we assume total recharge potential to be 4200 cm/day. Soil depths are not uniform over the catchment area (Figure 18), and Table 7 shows that hydraulic conductivity at shallow depths are two orders of magnitude greater. With this in mind a K_{SAT} value of 2×10^{-5} m/s would be approximately 200 cm/day, a much higher rate of infiltration. Under this assumption of extremely high infiltration rates and water available for recharge the entire yearly precipitation total that falls on WS07 would go to groundwater recharge. We know this is not the case. Where does the water go then? Assuming that the bedrock permeability is much lower than the overlying soil permeability lateral flow, similar to the fill and spill hypothesis, along this interface is likely. Lateral flow is expected in areas with a high contrast of permeabilities and therefore would be expected in areas of shallow soils shown in Figure 18 and their higher relative K_{SAT} values. A small portion of water may infiltrate into bedrock fractures but a quantitative understanding of that is beyond the scope of this research. Areas of shallow soil adjacent to the WS07 stream with high relative conductivities are likely sources of stream discharge routing infiltrated water laterally towards the stream.

7. Discussion

The movement of water through the subsurface is a function of the watershed topography, both surface and bedrock. These topographical controls are subject to the physical laws that govern water flow through the subsurface and help determine flowpath lengths. Subsurface flow is most notably dependent on local soil properties, head gradients, and the level of subsurface saturation. To adequately explain these complex and often interconnected processes it is helpful to present a conceptual drawing of the watershed (Figure 21).

Precipitation vertically infiltrates the soil profile at a rate, as explained above, determined by Darcy's law with permeability of the soil and the head gradient the principle components in this functional relationship. Early vertical infiltration is dominated by capillary flow of the soil with the force of gravity dominating at longer time scales. Vertical infiltration will continue until the water reaches the saturated zone or when lateral flow is initiated through abrupt decreases in permeability. These can occur in heterogeneous soils, within the profile, and at the soil/bedrock interface.

As water in the *Upper* section of WS07 vertically infiltrates into the subsurface it passes through increasingly less permeable soils. Vertical flow persists until a limiting permeability is met, in this case the soil/bedrock interface where a sharp decrease in permeability is thought to exist, forcing infiltrated water laterally. From our knocking pole soil depth experiments we found that the upper boundary of WS07 the soils are relatively deep compared to the mid-slope where soils are less than one meter on average. This mid-slope area will produce laterally flow earlier, all else similar, than the upper boundary as it takes less time to reach the soil/bedrock interface. This suggests that this zone is the primary zone of hillslope discharge to the stream and corresponds to where we found significant lateral inflows contributing to the stream discharge (15% and 16% of total stream discharge). Not only are the soils more shallow in this mid slope region but the surface topography has the highest slope angle as well. If we assume that the bedrock topography loosely mimics the surface topography we can then assume a higher flux. The topographic slope angle increases

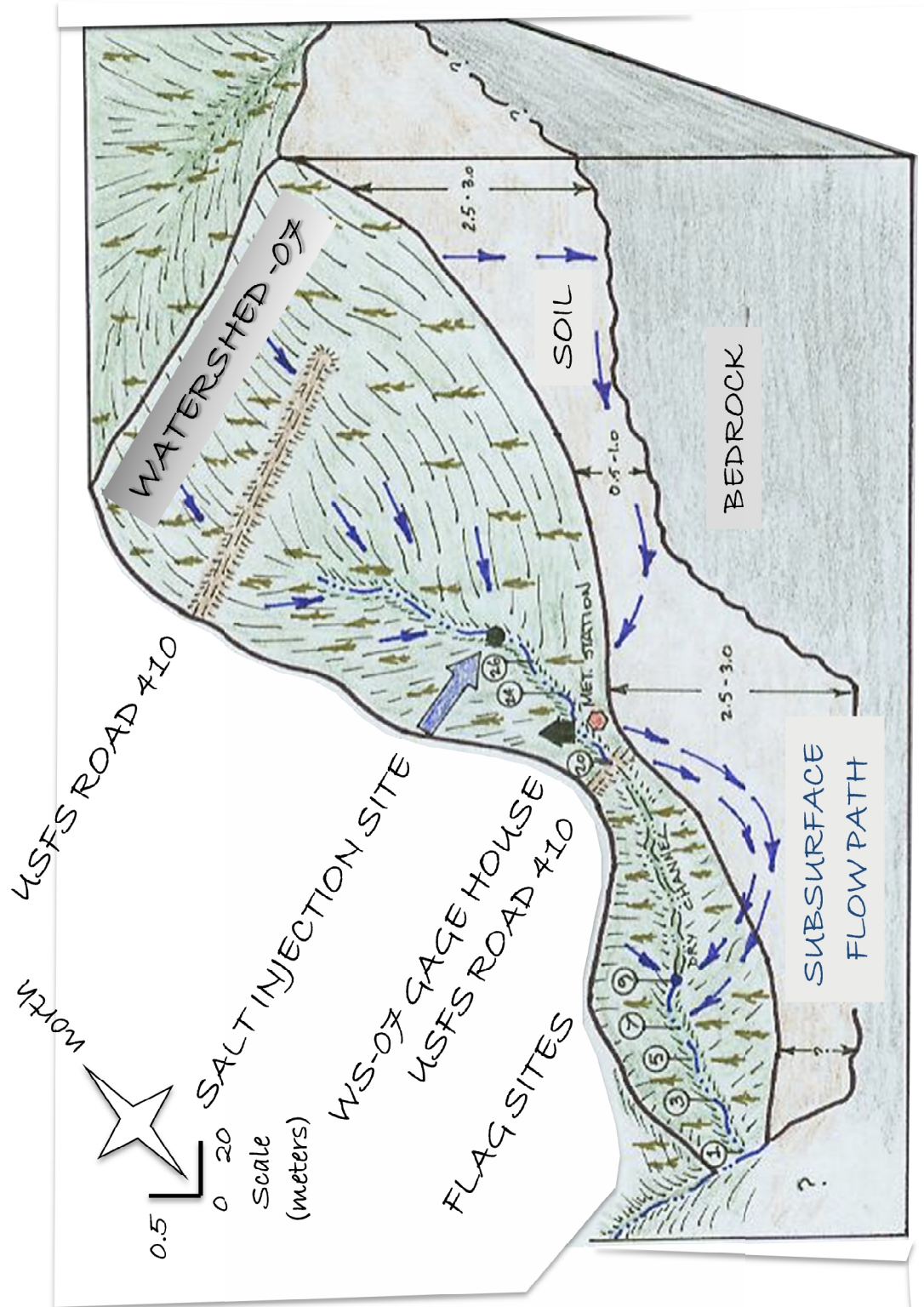


Figure 21: Conceptual drawing of subsurface water flow within WS07 at the H.J. Andrews Experimental Forest.

the force of gravity on horizontal flow, further increasing hillslope water discharge to the stream. The upper boundary area with deep soils do become saturated in time and lateral flow does occur, this area then helps to sustain high winter flows and contributions to baseflow as the water table recedes during the summer months. Figure 21 depicts this mid-slope zone as the primary generator of lateral flow and stream discharge. Not surprisingly, this area coincides with the stream's surface water origin and the primary zone of lateral inflows augmenting stream discharge (Figure 2).

Further down the slope the soils become deeper and forcing less water laterally to the stream. During the wet season the water table is high and is in direct connection to the surface water making a consistently present surface water source within the stream. As the summer progresses and the water table recedes lower into the soil profile, the WS07 stream becomes a losing stream. The resulting disconnection of the water table and the stream causes the surface water to go entirely subsurface for an extended section of the stream.

Our results from the salt injection lead us to believe that there are multiple flowpaths that this water takes before it reemerges downstream. There seems to be an interaction with a subsurface water source that did not have its origins within the *Upper* stream channel and thus diluting the salt signal in the *Lower* section. Additionally, there exists a longer flowpath that mixes with a higher volume of subsurface water, which connects the *Upper* surface water with the reemergence point at flag 9. Flag 9 has a much lower salt concentration and a much lower temperature regime, suggesting that the bulk of the water emerging at flag 9 is not 'hyporheic' but rather groundwater in the more pure form, i.e. water discharging from a subsurface source rather than water that at one point helped comprise the surface water discharge somewhere upstream. Directly downstream of flag 9, flag 8-1 demonstrate a more 'hyporheic' signal with a stronger salt concentration and warmer temperature regime. A longer flowpath with less interaction with groundwater and comprised of more *Upper* surface water is therefore suggested.

The groundwater source is, however, unknown. We are uncertain of its origins, i.e. are we sampling deeper groundwater discharging from a bedrock aquifer or is the groundwater derived from a more shallow source from the adjacent watersheds 06 and 08 and draining into the WS07 stream? Additionally, the bedrock permeability contrasts with the overlying soil is not entirely clear thus throwing into question the assumption that lateral flow is induced at the soil/bedrock interface. Preliminary drilling into the bedrock of WS07 and other watersheds within the Andrews has suggested that the bedrock near the soil interface is quite fractured. The fractured nature could provide conduits of preferential flow that route water to the deeper aquifer and add an additional complexity to subsurface water flow such as increased vertical flow and less of the fill and spill mechanism presented earlier. The bedrock connection with shallow subsurface flow is a necessary area for further work. Instead of assuming bedrock as an impermeable layer that has no hydrological implications to surface water production, future work with an alternative hypothesis should seek to question this impermeability and lack of connectivity.

8. *Conclusions*

The research and results presented the WS07 headwater catchment within the context of how the catchment receives and delivers energy to the stream through an in-depth focus on distributed stream temperature monitoring and modeling. Additionally, we examined subsurface delivery of water and how soil properties effect subsurface routing. The conclusions found in this research project are described below.

Stream temperature measurements were carried out by DTS which allowed us to observe at high spatial and temporal resolution the intimate energy relationship between the stream and its environment. We measured stream temperatures of a single stream that acted as two separate streams due to its unique subsurface section and distinct temperature regimes. DTS was employed over a 4 day period in July 2010 and we performed an energy balance computation to examine the controls on stream

temperature. Using a physically based energy balance modeling approach we modeled the stream as two sections, each with distinct vegetation and geomorphic attributes. The two sections had very different energy fluxes that contributed to stream temperature. The sum of the energy fluxes going to heat the stream were 302 W/m² and 210 W/m² for the upper and lower section respectively.

The upper section with a less dense forest cover canopy to block incident solar radiation making, as shown in the literature, solar radiation the largest energy source to directly affect stream temperatures at 53% of total flux. Both atmospheric longwave and back longwave radiation had higher magnitudes of energy but they offset each other. Landcover longwave radiation did contribute significantly, 25% of total energy flux going to heat the stream. Evaporative cooling and sensible heat flux had similar magnitudes and offset each other. This finding is not surprising and typical of other streams in the region under shade (Johnson, 2004).

The lower section flowed through a more dense riparian cover of old growth and as a result the solar radiation incoming flux was significantly reduced, as compared to the upper section. Solar radiation accounted for only 24% of total flux. As a result of the vegetation cover however, longwave radiation became the primary flux of energy to the stream at 35%. Energy results of both sections were in line with the DTS observations that showed larger temperature variation in the upper section than the lower section.

Contributing to the energy balance results and the distinct temperature regimes of the two sections, salt tracer results showed that the lower section had a high volume of groundwater lateral inflows contributing to discharge. Admittedly the vast majority of the inflow volume occurred near the reemergence point at flag 8 where discharge doubled in volume compared to the upper section where the stream went subsurface. The high volume of lateral inflows muted the temperature signal and increased stream discharge volume requiring increased energy fluxes to affect the in-stream temperatures. The upper section had two distinct lateral inflow locations, they accounted for 15% and 16% of total discharge. A similar percentage of lateral inflow

to the stream by localized near stream hillslope sources has been found in other catchments as well (McGuire et al., 2007).

The use of DTS to quantify lateral inflow source has been shown to be effective (Huff, 2009, Westhoff et al., 2007, and Selker et al., 2006b). However, propagation of uncertainty within the measurement outputs can lead to errors. We found that total measurement uncertainty associated with DTS, after careful and rigorous post-collection calibration methods, was on the order of 0.21 °C. With this uncertainty included we showed that widespread application of DTS for the quantification of lateral inflows, while still an effective tool, a few assumptions must be followed in order to be able to successfully defend subsequent findings. These include: areas of interest have to exhibit distinct temperature differences in upstream and downstream profiles otherwise the corresponding uncertainty completely masks the result; no significant outside sources of temperature fluctuation may be observed, i.e. energy influxes between the upstream and downstream sections must be identical (or nearly); and groundwater inflows must appreciably and abruptly change the in-stream temperature from upstream and downstream. Where temperature profiles are not significantly different from each other we showed that uncertainty propagation can lead to variability in lateral inflow quantification of upwards to +/- 10-15 l/s. We also caution that high gradient small streams with high variability in depth profiles and in-stream woody debris present can lead to observed temperature differences that may be a result of out-of-water segments of cable. These sections must be accounted for either by visual inspection or by an automated method, for example by the one presented here.

Through extensive field work to map the bedrock topography and glean soil properties we presented soil depths and some basic principles regarding subsurface infiltration and lateral flow mechanisms. WS07 soils show a tendency for K_{SAT} to decrease with depth. Decreasing hydraulic conductivities with depth is similar to various other findings that K_{SAT} decreases exponentially with depth due to compaction and the fining of soils. Routing of infiltrated water laterally will occur where areas that

have distinct permeability contrasts, i.e. at the soil/bedrock interface. Given that areas with shallow soils have higher K_{SAT} at this interface relative to areas of deeper soils we would expect these areas to exhibit strong lateral flow tendencies and follow the fill and spill hypothesis. These are areas of shallow soil adjacent to the WS07 which are likely large sources of stream discharge

This research sought to understand stream temperature and subsurface processes and how they relate to headwater catchment function. We perform extensive field work to determine soil properties and quantify soil depths spatially within WS07. This field work gave us a foundation to base our interpretations of source water contributions and lateral inflow on while establishing essential soil properties that gave validity to our calculations and assumptions. Additionally we characterized the stream temperature response to energy inputs through distributed temperature sensing and extensive modeling effort. Vegetation riparian cover for low volume high gradient streams is a significant deterrent to solar radiation influx, the primary control on stream temperature augmentation.

Further work determining the extent of connectivity of bedrock on subsurface water transport mechanisms is suggested to include focused hydrometric studies on soil water development and the fractured bedrock, especially in shallow soils areas adjacent to the WS07 stream.

9. References

- Adams, R.K., Spotila, J.A. (2005). The form and function of headwater streams based on field and modeling investigations in the Southern Appalachian Mountains. *Earth Surface Processes and Landforms*, 30, 1521-1546.
- AFL Telecommunications, Duncan, SC, USA.
- Allan, J.D. (1995). *Stream Ecology: Structure and Function of Running Waters*. New York: Chapman & Hall.
- Anderson, M.G., Kneale, P.E. (1982). The influence of low angled topography on hillslope soil water convergence and stream discharge. *Journal of Hydrology*, 57, 65-80.
- Berman, E.S.F., Gupta, M., Gabrielli, C., Garland, T., McDonnell, J.J. (2009). High-frequency field deployable isotope analyzer for hydrological applications. *Water Resources Research*, 45.
- Beschta, R.L. & Weathered, J. (1984). TEMP-84. A computer model for predicting stream temperatures resulting from the management of streamside vegetation. Watershed Systems Development Group, Ft. Collins, Colorado. U.S. Department of Agriculture, Washington, D.C., WSDG-AD-00009.
- Beven, K.J., Kirkby, M.J., (1979). A physically based variable contributing area model of basin hydrology. *Hydrological Sciences Bulletin*, 24 (1), 43–69.
- Beven, K.J. (1982b) On subsurface stormflow: an analysis of response times. *Hydrological Science Journal*, 27(4), 505-521.
- Beven, K. J. (1984). Infiltration into a class of vertically nonuniform soils. *Hydrological Science Journal*, 29(4), 425-434,.
- Boderie, P., Dardengo, L. (2003). Warmtelozing in oppervlaktewater en uitwisseling met de atmosfeer, Report Q3315, WL|Delft Hydraulics.
- Boyd, M., & Kasper, B. (2003). Analytical methods for dynamic open channel heat and mass transfer: methodology for HeatSource Model version 7.0. Retrieved from <http://www.deq.state.or.us/WQ/TMDLs/tools.htm>.
- Brososke, K.D., Chen, J., Naiman, R.J., Franklin, J.F. (1997). Harvesting effects on microclimatic gradients from small streams to uplands in western Washington. *Ecological Applications* 7:1188-1200.
- Brown, G.W., (1969). Predicting temperatures of small streams. *Water Resources Research* 5:68-75.
- Brown, G.W., Krygier, J.T. (1970). Effects of clear-cutting on stream temperature. *Water Resources Research* 6:1133-1139.
- Brutsaert, W. (2007). *Hydrology: An introduction*. Cambridge University Press, Cambridge, UK.
- Chen, J., Franklin, J.F., Spies, T.A. (1995). Growing season microclimatic gradients from clearcut edges into old-growth douglas-fir forests. *Ecological Applications* 5:74-86.
- Collier, M.W. (2008). Demonstration of fiber optic distributed temperature sensing to differentiate cold water refugia between groundwater inflows and hyporheic exchange (MS Thesis). Oregon State University.

- Constantz, J. (2008). Heat as a tracer to determine streambed water exchanges. *Water Resources Research*, 44.
- Davies-Colley R.J., Payne, G.W., van Elswijk, M. (2000). Microclimate gradients across a forest edge. *New Zealand Journal of Ecology* 24:111-121.
- Danehy, R.J. & Kirpes, B.J. (2000). Relative humidity gradients across riparian areas in eastern Oregon and Washington forests. *Northwest Science* 74:224-233.
- Davis, J.C., 1986. *Statistics and Data Analysis in Geology*, 2nd ed. John Wiley and Sons, New York.
- Day, P.D. (1965). Particle fractionation and particle size analysis. In *Methods of Soil Analysis*, Black, C.A. (ed). American Society of Agronomy, Inc. Madison, Wisconsin, USA, 545:566.
- Dent, L., Vick, D., Abraham, K., Schoenholtz, S., Johnson, J. (2008). Summer Temperature Patterns in Headwater Streams of the Oregon Coast Range. *Journal of the American Water Resources Association*, 44(4):803-813.
- Dietrich, M., Anderson, H.N. (2000). The Invertebrate Fauna of Summer-Dry Streams in Western Oregon. *Archiv für Hydrobiologie*, 147(3):273-295.
- Dietrich, W.E., Dunne, T. (1993). The channel head. pp. 175–219 in *Channel network hydrology*, Beven, K., and M.J. Kirkby (eds.). John Wiley and Sons, New York.
- Dyrness, C. T. (1969), Hydrologic properties of soils on three small watersheds in the western Cascades of Oregon, Res. Note PNW-111, Pac. Northwest For. and Range Exp. Stn., For. Serv., U.S. Dep. of Agric., Portland, Oregon.
- Dyrness, C.T., Hawk, G. (1972). Vegetation and soils of watersheds 2 and 3. H. J. Andrews Experimental Forest. Coniferous Forest Biome Intern. Rep. 49.
- Evans, E.C., McGregor, G.R., Petts, G.E. (1998). River energy budgets with special reference to river bed processes. *Hydrological Processes*, 12(4), 575-595.
- Forsman, E.D., Meslow, E.C., Strub, M.J. (1977). Spotted Owl Abundance in Young versus Old-Growth Forests, Oregon. *Wildlife Society Bulletin* 5(2), 43-47.
- Gomi, T., Sidle, R.C., Richardson, J.S. (2002). Understanding processes and downstream linkages of headwater systems. *BioScience* 52: 905–916.
- Hack, J.T., Goodlett, J.C. (1960). Geomorphology and Forest Ecology of a Mountain Region in the Central Appalachians. U.S. Geological Survey: Washington, D.C. 66.
- Harr, R. D. (1977), Water flux in soil and subsoil on a steep forested slope, *Journal of Hydrology*, 33, 37– 58.
- Herrick, J.E., Jones, T.L. (2002). A dynamic cone penetrometer for measuring soil penetration resistance. *Soil Science Society of America Journal*, 66(4), 1320:1324.
- Hewlett, J.D., Hibbert, A.R. (1967). Factors affecting the response of small watersheds to precipitation in humid areas, in *International Symposium on Forest Hydrology*, 275-290, Pergamon Press, New York.
- Horton, R.E. (1945). Erosional development of streams and their drainage basins: hydrophysical approach to quantitative morphology. *Bulletin of the Geological Society of America* 56: 275–370.
- Huff, J.A. (2009). Monitoring river restoration using fiber optic temperature measurements in a modeling framework (MS Thesis). Oregon State University.

- Jones, J.A. (2000), Hydrologic processes and peak discharge response to forest removal, regrowth, and roads in 10 small experimental basins, western Cascades, Oregon, *Water Resources Research* 36, 2621–2642.
- Johnson, S.L. and Jones, J.A. (2000). Stream temperature responses to forest harvest and debris flows in western Cascades, Oregon. *Canadian Journal of Fisheries and Aquatic Science* 57(2), 30–39.
- Johnson, S.L., 2004. Factors influencing stream temperatures in small streams: substrate effects and a shading experiment. *Canadian Journal of Fisheries and Aquatic Sciences* 61:913-923
- King, J.P., Smith, D.F., Richards, K., Timson, P., Epworth, R.E., Wright, S. (1987). Development of a coherent OTDR instrument," *Journal of Lightwave Technologies*, vol. LT-5, pp. 616–624.
- Kragas, T.K., Williams, B.A., Myers, G.A. (2001). The optic oil field: deployment and application of permanent in well fiber optic sensing systems for production and reservoir monitoring. Paper SPE 71529 presented at the SPE Annual Technical Conference and Exhibition, New Orleans.
- Larson, L.L., & Larson, S.L. (1996). Riparian shade and stream temperature: a perspective. *Rangelands* 18:149-152.
- Legard, H. A., and L. C. Meyer (1973), Soil Resource Inventory, Atlas of Maps and Interpretive Tables, Willamette National Forest, Pac. Northwest Region, U.S. For. Serv., Portland, Oreg.
- Likens, G.E., Bormann, F.H., Pierce, R.S., Eaton, J.S., Johnson, N.M. (1977). Biogeochemistry of a forested eco- system. Springer-Verlag, New York, New York, USA.
- MacDonald, L.H., Coe, D. (2007). Influence of headwater streams on downstream reaches in forested areas. *Forest Science* 53(2):148-168.
- May, C.L., Gresswell, R.E. (2004). Spatial and temporal patterns of debris flow deposition in the Oregon Coast Range, U.S.A. *Geomorphology* 57:135–149.
- McGuire, K.J., Weiler, M., McDonnell, J.J., (2007). Integrating tracer experiments with modeling to assess runoff processes and water transit time. *Advances in Water Resources*, 30(4): 824-837.
- McGuire K.J., McDonnell J.J., Weiler M., Kendall C., Welker J.M., McGlynn B.L. (2005). The role of topography on catchment-scale water residence time. *Water Resources Research* 41(5):W05002.
- Meyer, J.L., Wallace, J.B. (2001). Lost linkages and lotic ecology: Rediscovering small streams. In *Ecology: Achievement and Challenge*, Press M.C., Huntly, N.J., Levin, S. (eds). Blackwell: Oxford; 295–317.
- Mobley, C.D. (1994). In *In Light and Water: Radiative transfer in natural waters*; Academic Press: New York.
- Mohseni, O., Stefan, H.G. (1999). Stream temperature/air temperature relationship: a physical interpretation. *Journal of Hydrology* 218:128-141.
- Montgomery, D.R., Dietrich, W.E. (1988). Where do channels begin? *Nature*, 336, 232–234.

- Montgomery, D.R., Dietrich, W.E. (1989). Source areas, drainage density, and channel initiation. *Water Resources Research* 25: 1907–1918.
- Montgomery, D.R., Foufoula-Georgiou, E. (1993). Channel network source representation using digital elevation models. *Water Resources Research*. 29:3925–3934.
- Monteith, J.L. (1981). Evaporation and surface temperature. *Quarterly Journal of the Royal Meteorological Society*, 107, 1–27.
- Monteith, J.L., Unsworth, M. (1990). Principles of environmental physics. 2nd ed. Arnold Press, London, UK.
- Moore, R.D. (2004b). Introduction to salt dilution gauging for streamflow measurement: Part I. *Streamline Watershed Management Bulletin* 7(4):20–23.
- Moore, R.D. (2004a). Introduction to salt dilution gauging for streamflow measurement Part II: constant rate injection. *Streamline Watershed Management Bulletin* 8 (1): 11.
- Moore, R.D., Wondzell, S.M. (2005). Physical hydrology in the Pacific Northwest and the effects of forest harvesting: A review. *Journal of the American Water Resources Association* 41:753–784.
- Moore, D.R., Spittlehouse, D.L., Story, A. (2005). Riparian microclimate and stream temperature response to forest harvesting: a review. *Journal of the American Water Resources Association*, 41(4), 813-834.
- Neilson, B.T., Hatch, C.E., Heng, B., Tyler, S.W. (2010). Solar radiative heating of fiber optic cables used to monitor temperatures in water. *Water Resources Research*.
- Oke, T.R., 1987. *Boundary Layer Climates* (Second Edition). Halsted Press, London, United Kingdom.
- Oregon Headwater Research Cooperative. (2010). Retrieved from September 09, 2010 <http://headwatersresearch.org>.
- Ozaki, N., Fukushima, T., Harasawa, H., Kojiri, T., Kawashima, K., Ono, M. (2003). Statistical analyses on the effects of air temperature fluctuations on river water qualities. *Hydrological Processes* 17: 2837–2853.
- Philip, J. (1957). The Theory of infiltration: sorptivity and algebraic infiltration equations. *Soil Science* 84(3), 257-264.
- Poole, G.C., & Berman, C.H. (2001). An ecological perspective on in-stream temperature: natural heat dynamics and mechanisms of human caused thermal degradation. *Environmental Management*, 27(6), 787-802.
- Prosser, I.P. (1996). Thresholds of channel initiation in historical and Holocene times, south-eastern Australia. In *Advances in Hillslope Processes*, Volume 2. Anderson M.G., Brooks S.M. (eds). John Wiley and Sons: Chichester; 687–708.
- Ranken D.W. (1974). Hydrologic properties of soil and subsoil on a steep, forested slope (MS Thesis). Oregon State University.
- Raynor, G.S. (1971). Wind and Temperature Structure in a Coniferous Forest and Contiguous Field. *Forest Science* 17:351-363.
- Reifsnyder, W.E., & Lull, H.W. (1965). Radiant Energy in Relation to Forests. *Technical Bulletin 1344*, USDA Forest Service, Washington D.C.

- Royle, A.G., Clausen, F.L., Frederiksen, P. (1981). Practical Universal Kriging and Automatic Contouring. *Geoprocessing*, 1, 377-394.
- Roth, T.R., Westhoff, M., Huwald, H., Huff, J., Rubin, J., Barrenetxea, G., Selker, J.S. (2010). Stream temperature response to three riparian vegetation scenarios using a distributed temperature validated model. *Environmental Science & Technology*.
- Rupp, D.E., Selker, J.S. (2005). Drainage of a horizontal Boussinesq aquifer with a power law hydraulic conductivity profile. *Water Resources Research*, 41, W11422.
- Sayde, C., Gregory, C., Gil-Rodriguez, M., Tufillaro, N., Tyler, S., van de Giesen, N., English, M., Cuenca, R., Selker, J.S. (2010), Feasibility of soil moisture monitoring with heated fiber optics, *Water Resources Research*, 46, W06201.
- Schumm, S.A. (1956). Evolution of drainage systems and slopes in badlands at Perth Amboy, New Jersey. *Bulletin of the Geological Society*, 67, 597–646.
- Selker, J. S., Duan, J., Parlange, J.Y. (1999). Green and Ampt infiltration into soils of variable pore size with depth, *Water Resources Research*, 35(5), 1685–1688.
- Selker, J.S., Keller, C.K., McCord, J.T. (1999). *Vadose Zone Processes*. CRC Press, Boca Raton, FLA.
- Selker, J.S., van de Giesen, N., Westhoff, M., Luxemburg, W.M.J., Parlange, M.B. (2006). Fiber optics opens window on stream dynamics. *Geophysical Resource Letters*, 33(24), 24401.
- Selker, J.S., Thevanaz, L., Huwald, H., Mallet, A., Luxemburg, W.M.J., van de Giesen, N. (2006). Distributed fiber optic temperature sensing for hydrologic systems. *Water Resources Research*, 42.
- Selker, J. S. (2008), Taking the temperature of ecological systems with fiber optics. *Eos Trans. AGU*, 89(20), 187.
- Shreve, R.W. (1969). Stream lengths and basin areas in topologically random channel networks. *Journal of Geology* 77, 397– 414.
- Sidle, R. C., Tsuboyama, Y., Noguchi, S., Hosoda, I., Fujieda, M., Shimizu, T. (2000), Streamflow generation in steep forested headwaters: a linked hydro-geomorphic paradigm. *Hydrological Processes*, 14, 369– 385.
- Sinokrot, B.A., & Stefan, H.G. (1993). Stream temperature dynamics: measurements and modeling. *Water Resources Research*, 29(7), 2299-2312.
- Sherrod, D.R., Smith, J.G. (2000). Geologic map of upper Eocene to Holocene volcanic and related rocks of the Cascade Range, Oregon. U.S. Geological Survey Geologic Investigations Series I-2569, 1:500,000.
- Spittlehouse, D.L., Adams, R.S., Winkler R.D. (2004). Forest, Edge, and Opening Microclimate at Sicamous Creek. *Research Report 24*, Res. Br., British Columbia Ministry of Forests, Victoria, B.C., Canada.
- Stevens, H.H., Ficke, J.F., Smoot, G.F. (1975). Water temperature, influential factors, field measurement and data presentation. in *US Geological Survey Tech of Water Resources Invest*, Book 1, Ch. D1.
- Stonestrom, D.A., & Constantz, J. (ed.). (2003). Heat as a tool for studying themovement of ground water near streams. USGS Circular 1260. USGS.

- Story, A., Moore, R.D., Macdonald, J.S. (2003). Stream temperatures in two shaded reaches below cut blocks and logging roads: downstream cooling linked to subsurface hydrology. *Canadian Journal of Forest Research* 33:1383-1396.
- Sullivan, K., and Adams, T.A. 1990. The physics of forest stream heating: 2. An analysis of temperature patterns in stream environments based on physical principles and field data. Weyerhaeuser Tech. Rep. 004-5002.90/2. Technology Center, Tacoma, Wa.
- Swanson, F.J., James, M.E. (1975). Geology and geomorphology of the H. J. Andrews Experimental Forest, Western Cascades, Oregon, Pacific Northwest Forest and Range Experimental Station, PNW-188.
- Trewartha, G.T. (1968). *An Introduction to Climate*. McGraw-Hill, New York.
- Tromp-Van Meerveld, H.J., McDonnell, J.J. (2006). Threshold relations in subsurface stormflow 2. The fill and spill hypothesis: An explanation for observed threshold behavior in subsurface stormflow. *Water Resources Research*.
- Tyler, S.W., Selker, J.S., Hausner, M.B., Hatch, C.E., Torgensen, T., Thodal, C.E. (2009). Environmental temperature sensing using Raman spectra DTS fiber-optic methods. *Water Resources Research*, 45.
- US EPA. (2006). Section 303(d) List Fact Sheet for OREGON_WATERS_US_EPA. Retrieved September 09, 2010, from http://oaspub.epa.gov/tmdl/state_rept.control?p_state=OR&p_cycle=2006
- Webb, B.W., & Zhang, Y. (1997). Spatial and seasonal variability in the components of the river heat budget. *Hydrological Processes* 11, 79–101.
- Wemple, B.C., Jones, J.A., Grant, G.E. (1996). Channel network extension by logging roads in two basins, western Cascades, Oregon. *Water Resources Bulletin*. 32:1195–1207.
- Westhoff, M.C., Savenije, H.H.G., Luxemburg, W.M.J., Stelling, G.S., van de Giesen, N.C., Selker, J.S. (2007). A distributed stream temperature model using high resolution temperature observations. *Hydrology and Earth System Sciences*, 11(4), 1469.
- Woods, R., Sivapalan, M., Duncan, M. (1995). Investigating the representative elementary area concept: An approach based on field data. *Hydrological Processes* 9:291–312.
- Young, K.A. (2000). Riparian Zone Management in the Pacific Northwest: Who's Cutting What? *Environmental Management* 26:131-144.

APPENDIX

TABLE A1				
ID	NAME	X Coordinate	Y Coordinate	Soil Depth (m)
0	15 1W	565566.6914	4901759.407	2.37
1	13 1E	565671.4086	4901733.419	2.67
2	11 1E	565692.9768	4901700.256	1.59
3	9 1E	565721.1521	4901692.846	1.26
4	7 1E	565765.2411	4901685.478	0.48
5	3 1E	565813.3626	4901661.258	1.6
6	5 1E	565778.4614	4901676.031	0.92
7	13 2W	565568.6834	4901705.881	1.56
8	13 1W	565598.6102	4901717.122	2.26
9	9 1W	565653.4784	4901652.256	2.02
10	7 1W	565688.9243	4901652.959	1.63
11	5 1W	565723.7102	4901634.129	1.26
12	3 2W	565708.5076	4901620.187	3.86
13	3 1W	565751.1977	4901627.636	3.32
14	15 2W	565531.5286	4901745.105	2.62
15	15	565608.8362	4901766.476	2.97
16	17	565594.9703	4901798.081	1.56
17	T1	565680.5211	4901670.968	1.47
18	11	565657.3903	4901692.05	1.62
19	13	565632.1419	4901733.459	3.83
20	9	565680.4188	4901685.482	1.49
21	T2	565688.9249	4901679.284	1.76
22	T3	565696.757	4901691.323	1.36
23	T4	565706.1892	4901697.833	1.64
24	T5	565716.3364	4901704.012	2.7
25	3	565784.5004	4901638.629	1.26
26	5	565748.593	4901656.866	2.09
27	1W	565787.0176	4901593.332	4.13
28	1	565815.2314	4901617.6	2.83
29	High West	565468.523	4901880.193	1.85
30	High Center	565544.715	4901915.676	0.81
31	High East	565609.854	4901926.115	1.9
32	Mid East	565630.008	4901889.687	2.3
33	Mid Center	565562.461	4901860.249	2.1
34	Mid West	565503.58	4901817.997	2.8
35	Low West	565509.369	4901794.487	2.25
36	Low Center	565581.503	4901831.856	1.7
37	Low East	565659.998	4901844.664	1
38	3-1E '09	565808.688	4901649.095	2.25
39	5-1E '09	565773.647	4901662.285	0.8
40	7-1E '09	565748.693	4901695.486	1.45

41	9-1E '09	565715.072	4901699.016	0.7
42	9-2E '09	565742.902	4901700.54	0.9
43	11-2E '09	565736.433	4901709.567	1.15
44	11-1E '09	565694.654	4901716.316	0.75
45	13-3E '09	565744.639	4901723.498	1.1
46	13-2E '09	565702	4901735.181	0.85
47	15-2E '09	565669.941	4901749.109	1.5
48	15-1E '09	565645.096	4901749.973	2
49	17-1E '09	565631.892	4901790.325	2.55
50	17-4E '09	565749.882	4901795.074	3.3
51	17-2E '09	565698.854	4901788.988	2.64
52	15-4E '09	565755.476	4901749.748	2.5
53	15-3E '09	565707.805	4901747.098	1.5
54	17-3E '09	565742.163	4901792.034	2.4
55	13-1E '09	565651.511	4901732.06	2.42
56	15-1E '09	565645.096	4901749.973	2

Table A2

ID	NAME	X Coordinate	Y Coordinate	Measurement Depth (cm)	K_{SAT} (m/s)
8	13 1W	565598.6102	4901717.122	-30	5.18E-05
14	15 2W	565531.5286	4901745.105	-30	6.50E-05
15	15	565608.8362	4901766.476	-38	3.00E-05
				-76	1.62E-05
16	17	565594.9703	4901798.081	-40	1.17E-04
				-80	3.97E-07
18	11	565657.3903	4901692.05	-38	1.40E-04
				-76	2.08E-08
23	T4	565706.1892	4901697.833	-38	3.77E-05
				-76	2.70E-04
27	1W	565787.0176	4901593.332	-38	1.07E-04
				-76	4.10E-05
22	T3	565696.757	4901691.323	-30	6.50E-05
40	7-1E '09	565748.693	4901695.486	-30	2.06E-04